AIP | Physics of Plasmas

The link between shocks, turbulence, and magnetic reconnection in collisionless plasmas

H. Karimabadi, V. Roytershteyn, H. X. Vu, Y. A. Omelchenko, J. Scudder, W. Daughton, A. Dimmock, K. Nykyri, M. Wan, D. Sibeck, M. Tatineni, A. Majumdar, B. Loring, and B. Geveci

Citation: Physics of Plasmas (1994-present) **21**, 062308 (2014); doi: 10.1063/1.4882875
View online: http://dx.doi.org/10.1063/1.4882875
View Table of Contents: http://scitation.aip.org/content/aip/journal/pop/21/6?ver=pdfcov
Published by the AIP Publishing

The link between shocks, turbulence, and magnetic reconnection in collisionless plasmas

H. Karimabadi,[1,2] V. Roytershteyn,[2] H. X. Vu,[2] Y. A. Omelchenko,[1,2] J. Scudder,[3] W. Daughton,[4] A. Dimmock,[5,6] K. Nykyri,[6,5] M. Wan,[7] D. Sibeck,[8] M. Tatineni,[9] A. Majumdar,[9] B. Loring,[10] and B. Geveci[11]
[1]*University of California, San Diego, La Jolla, California 92093, USA*
[2]*SciberQuest, Inc., Del Mar, California 92014, USA*
[3]*University of Iowa, Iowa City, Iowa 52242, USA*
[4]*Los Alamos National Laboratory, Los Alamos, New Mexico 87545, USA*
[5]*Aalto University, Espoo, Finland*
[6]*Embry Riddle Aeronautical University, Florida 32114, USA*
[7]*University of Delaware, Newark, Delaware 19716, USA*
[8]*NASA Goddard Space Flight Center, Greenbelt, Maryland 20771, USA*
[9]*San Diego Supercomputer Center, La Jolla, California 92093, USA*
[10]*Lawrence Berkeley National Laboratory, Berkeley, California 94720, USA*
[11]*Kitware, New York 12065, USA*

(Received 26 February 2014; accepted 7 May 2014; published online 18 June 2014)

Global hybrid (electron fluid, kinetic ions) and fully kinetic simulations of the magnetosphere have been used to show surprising interconnection between shocks, turbulence, and magnetic reconnection. In particular, collisionless shocks with their reflected ions that can get upstream before retransmission can generate previously unforeseen phenomena in the post shocked flows: (i) formation of reconnecting current sheets and magnetic islands with sizes up to tens of ion inertial length. (ii) Generation of large scale low frequency electromagnetic waves that are compressed and amplified as they cross the shock. These "wavefronts" maintain their integrity for tens of ion cyclotron times but eventually disrupt and dissipate their energy. (iii) Rippling of the shock front, which can in turn lead to formation of fast collimated jets extending to hundreds of ion inertial lengths downstream of the shock. The jets, which have high dynamical pressure, "stir" the downstream region, creating large scale disturbances such as vortices, sunward flows, and can trigger flux ropes along the magnetopause. This phenomenology closes the loop between shocks, turbulence, and magnetic reconnection in ways previously unrealized. These interconnections appear generic for the collisionless plasmas typical of space and are expected even at planar shocks, although they will also occur at curved shocks as occur at planets or around ejecta. © *2014 AIP Publishing LLC*. [http://dx.doi.org/10.1063/1.4882875]

I. INTRODUCTION

There is growing evidence that magnetic reconnection and turbulence are intimately connected in magnetized plasmas (e.g., Refs. 1–5 and references therein). However, the link between shocks and these two processes has been less clear. We explore this connection using global kinetic simulations of the Earth's bow shock, and in the process address a number of puzzling observations. Due to the availability of *in situ* measurements,[6] the Earth's bow shock is the most studied example of collisionless shocks. The bow shock is a curved shock formed due to interaction of the supermagnetosonic solar wind with the Earth's magnetic dipole which acts as a barrier. The shocked solar wind is called the magnetosheath and is bounded by the magnetopause which diverts the flow.

Observations, along with theory and simulations, have provided considerable insight into the physics of collisionless fast shocks. The curved nature of the bow shock means that at a given instant, there are regions with quasi-parallel $Q_{\parallel}$ ($0^\circ \le \theta_{BN} \le 45^\circ$ and quasi-perpendicular $Q_{\perp}$ ($45^\circ \le \theta_{BN} \le 90^\circ$) geometries. Here, θ_{BN} is the angle between the shock normal and the incident magnetic field. In the quasi-parallel case, there exists a significant number of ions reflected from the shock that reach to large distances upstream. The relative streaming between these ions and the incoming plasma excites instabilities which generate low frequency waves that can grow to large amplitudes, giving rise to steepened fronts called magnetosonic shocklets and short large-amplitude magnetic structures (SLAMS) as well as other nonlinear structures such as cavitons (see review in Ref. 6). These structures are convected back into the shock and contribute to generation of turbulence in the magnetosheath.

There are also reflected ions associated with quasi-perpendicular shocks, but these ions remain confined to the foot of the shock, leading to shock reformation on the gyro-scales of the ions for a certain range of parameters (e.g., Ref. 7). There can also be turbulence downstream of quasi-perpendicular shocks due to temperature anisotropy driven instabilities with magnetic fluctuation levels $B_{rms}/B_o \sim 0.1$ as compared to $B_{rms}/B_o \sim 1$ downstream of quasi-parallel shocks.[8]

Despite this progress, a number of important issues remain. One issue of considerable debate is whether bow

shock turbulence has significant large scale consequences, especially since the turbulence is initiated on ion scales. In particular, observations have shown evidence of anomalous flows in the magnetosheath. Examples include observations of fast jets (see Refs. 9, 10, and references therein) and sunward flows (see Ref. 11 and references therein). The origin of such flows and their impact on the magnetosphere remain controversial. Since solar wind has embedded discontinuities that frequently impinge on the magnetosphere, models to explain these anomalous flows fall into two general categories: those that invoke the role of discontinuities and those that rely on the physics of the bow shock itself. Similarly, observations have reported reconnecting current sheets in the quasi-parallel magnetosheath.[12,13] These are difficult measurements and confirmation through simulations would be helpful but no evidence for such current sheets have yet been reported in the global simulations.

Simulations provide a global view of the magnetosphere and its dynamical evolution. In order to address the above issues, and to gain a better understanding of the turbulence associated with the bow shock, we use global hybrid and global fully kinetic simulations that capture the self-consistent formation of the bow shock and its associated turbulence. Most studies to date have focused on the upstream region of the $Q_{\parallel}$ bow shock, called the ion foreshock. We use our simulations to compare and contrast the nature of fluctuations/turbulence in the ion foreshock, $Q_{\parallel}$ magnetosheath, and $Q_{\perp}$ magnetosheath and their large scale consequences. We have run the simulations to a factor of $\sim$9 times longer than most previous studies in order to gain insight into the evolution of turbulence in time. Through these simulations, we find that the $Q_{\parallel}$ magnetosheath turbulence is much stronger than either that in the foreshock or in the $Q_{\perp}$ magnetosheath. We demonstrate, for the first time, that this enhanced level of turbulence leads to generation of reconnecting current sheets and formation of magnetic islands. This finding establishes the link between shocks, turbulence, and reconnection. This result is consistent with observations of reconnection in the quasi-parallel magnetosheath,[12,13] where, however, no search for magnetic islands was performed. In 3D, magnetic islands correspond to flux ropes. In the remainder of this paper, we will use the term magnetic islands and flux ropes interchangeably. Since some of the flux ropes reach tens of ion inertial length, we expect a dedicated observational search for flux ropes in the magnetosheath to yield many examples. One possibility to search for such flux ropes in the data may be through the use of the Grad-Shafranov reconstruction technique.[14,15]

The simulations also enable us to address large scale consequences of turbulence in the magnetosphere. We examined the possibility that foreshock turbulence, rather than interaction of solar discontinuities with the magnetosphere, could cause anomalous flows. We show that turbulence causes corrugation of the shock surface which in turn gives rise to collimated, high velocity plasma jets inside the magnetosheath. This is in agreement with the model originally proposed by Hietala *et al.*[9] and the properties of the jets are found to be consistent with high velocity magnetosheath flows recently reported in the observations.[9,10] The jets have high dynamical pressure and we show that upon reaching the magnetopause they can at times trigger so-called flux transfer events.[16]

Next, we considered whether the jets, which penetrate into the magnetosheath, can trigger sunward flows. Such a connection was proposed by Shue *et al.*[11] who attributed the origin of the sunward flow to the interaction of a jet with the magnetopause, which in turn would cause the magnetopause to rebound, creating a sunward motion. However, we find sunward flows in the vicinity of many jets that terminated in the magnetosheath far from the magnetopause. A careful examination of the time history of the flow reveals a complex process that would have been difficult to uncover in observations. In this process, the jets "stir" the magnetosheath, creating large scale disturbances and pushing the ambient low density plasma and the embedded magnetic field. The plasma in the sunward flow regions is not the plasma in the jets that was deflected, rather it is the plasma accelerated by thermal and dynamical pressure that develop because of the jets. In other words, the energy of the jets is convected into sunward flow rather than the deflection of the jets themselves. This energy conversion can give rise to sunward flows that extend tens and even hundreds of ion inertial length into the solar wind, well past the nominal position of the bow shock. The strong turbulence in the magnetosheath also gives rise to regions where the magnetic field during anti-sunward interplanetary magnetic field (IMF) orientation can point sunward in the magnetosheath. This is another testable prediction for observations.

Another consequence of the jets is found to be the nonlinear formation of large scale vortices in the magnetosheath. These vortices are driven due to turbulence and are to be distinguished from the usual Kelvin-Helmholtz driven vortices along the flanks of the magnetopause (Refs. 17, 18, and references therein).

Although these results were obtained from simulations of the bow shock, which is curved, similar effects are also expected at planar shocks. For example, the current sheets formed downstream of the quasi-parallel shocks is due to the strength of the turbulence, rather than any physics tied to the curvature of the shock. Similarly, the rippling of the surface of the shock is due to interaction of the shock with the steepened fronts getting convected back into it, an effect that is also present in planar shocks. The paper concludes with the discussion of the implications of these findings for the general understanding of plasmas and draws the link between shocks, reconnection and turbulence.

II. SIMULATION SETUP

Our hybrid simulation code is H3D,[19–21] a massively parallel hybrid code with a stretched mesh capability. Although we have conducted 3D global simulations of the magnetosphere,[20,21] here we will focus on 2D simulations for three reasons: (a) One of the key issues considered is whether the shock generated turbulence can lead to formation of reconnecting current sheets. The identification of reconnection in 3D remains a subject of active research and is still not completely resolved. (b) Confirmation of the

formation of reconnection sites observed in our global hybrid simulations through equivalent fully kinetic global simulations can only be done in 2D since 3D global fully kinetic simulations will remain out of reach in the foreseeable future. (c) We have conducted an extensive parameter study to identify the most interesting regimes which serve as conditions for 3D simulations to be published elsewhere.

Distances are normalized to ion skin depth d_i, time is normalized to ion cyclotron frequency Ω_{ci}, magnetic field is normalized to upstream magnetic field B_o, density is normalized to upstream density N_o, and velocity is normalized to the Alfvén speed $V_A = B_o/(4\pi N_o m_i)^{1/2}$, where m_i is the ion mass. The ratio of plasma to ion cyclotron frequency is set as 6000 and the ions and electrons are taken to have the same temperature $T_i = T_e$ for these runs. The Alfvénic Mach number is given by $M_A = V_{sw}/V_A$, where V_{sw} is the solar wind speed. We use a polytropic electron model with γ_e of 5/3 and 7/6, with the latter being suggested as more appropriate for shock physics.[22,23] The de Hoffmann-Teller cross shock potential under polytropic electron closure is proportional to $\gamma_e/(\gamma_e - 1)[kT_e]$. Thus using the more nearly correct γ_e for solar wind thermal electrons[22,23] of 7/6 leads to a larger de Hoffmann-Teller potential in hybrid simulations, raising the potential coefficient to 7 versus 5/2 for γ_e of 5/3.

We have conducted large number of hybrid simulations covering a range of D_p of 40 to the Earth's size of 600 d_i, plasma beta of 1 to 4, Alfvénic Mach number M_A of 4 to 12, IMF angle of 0° to 90°, and IMF B_z/B_o of 0 to 1. This range of parameters is not meant to be exhaustive but does represent a good coverage of the relevant parameter space. Here, D_p is the nose position of the magnetopause normalized to ion inertial length, which has been shown to be a good way to characterize the type of magnetospheric structure as a function of dipole strength.[24] We have also examined the effects of (i) spatial resolution by varying the grid from $0.25d_i$ to $1d_i$, (ii) particle per cell by considering a range of 10 to 200, (iii) and resistivity by considering different models such as no imposed resistivity, and several models based on gradients of magnetic field. We have found no significant effect of the resistivity on the physical processes considered here. However, care is required in general since use of large uniform resistivity as is done in some studies can lead to excess heating of the magnetosheath. We will focus this paper around the runs listed in Table I that are from converged solutions.

The simulation setup is similar to that used in global MHD simulations and consists of a magnetic dipole embedded in a uniform solar wind plasma which is continually injected from the left boundary. Mirror dipole is used to ensure the magnetic field is just the IMF field at the injection boundary. This reduces magnetic field perturbations at the injection boundary. All other boundaries use open boundary conditions. As in global MHD simulations, an inner boundary is placed around the Earth to limit the Alfvén speed from reaching relativistic values. Two particle boundary conditions are implemented: reflecting and absorbing. The dipole can also be ramped up in time, although we have not found significant differences compared to the case where the dipole is initialized at full strength at the start of the simulation. As the solar wind plasma interacts with the dipole, the magnetosphere forms in time. In 2D, the dipole is a line dipole in order to have a divergence free field.

TABLE I. List of parameters for the global hybrid simulation runs shown in this paper. The number of particles per cell was 200. The spatial resolution was $0.5d_i$ except for runs 1, 5 ($1d_i$) and run 6 ($0.25d_i$).

Run	x_{max}	y_{max}	D_p	$IMFB_z$	M_A	IMF_1	IMF_2	t_{flip}
1	2048	8192	100	0	8	−45°	10°	90
2	2048	4096	100	0	8	10°	10°	N/A
3	2048	4096	100	0	8	−45°	10°	90
4	8192	8192	300	0	10	−45°	10°	150
5	2048	4096	100	0.6	8	10°	10°	N/A
6	512	512	50	0.6	8	10°	10°	N/A
7	4096	2048	150	0.6	10	10°	10°	N/A

III. COMPARISON OF THE TURBULENCE REGIONS

Figure 1 shows the intensity plot of magnetic field at three different times for run 1 where the IMF direction changes at the injection boundary from −45° to 10° at $\Omega_{ci}t = 90$. This launches a rotational discontinuity (RD) that propagates towards the magnetosphere. The RD eventually runs into the reflected ions in the ion foreshock before reaching the bow shock. The time evolution of this interaction is shown in Figure 2 where we show a segment of the simulation zoomed in around the RD-reflected ion interaction region, along with 1D cuts of several parameters at $y = 3100d_i$. Figure 2 shows evidence for particles following the field lines across the RD into the upstream region. An observational evidence for this effect would be particles on magnetic field lines that do not point at the bow shock. Figure 2 also shows formation of at least three nonlinear structures: a fast shock, a cavity with hot plasma with depleted plasma density, and an anisotropic RD. The RD is seen to separate in time from the shockfront as expected.

A. Formation of the "foreshock bubble"

The interaction of an RD with shock reflected ions was shown to lead to a compound structure referred to as the foreshock bubble (FB) which consists of a fast magnetosonic shock attached to a very hot, low density cavity behind it.[25,26] The solution found here differs from the example of FB in Ref. 25 in at least two important aspects. First, the structure in Fig. 2 is more consistent with a localized front such as a shocklet than a shock since the plasma state behind it goes back to the solar wind conditions as evidenced from the 1D cut of plasma variables (e.g., Figures 2(d) and 2(j)). Second, the cavity is seen to remain much smaller than the extent of the shockfront in y and does not grow much in time (Figures 2(a)–2(c)). In contrast, in the case of FB in Ref. 25, the cavity covers almost the entire extent of the area behind the shock. Given these differences, we have labeled this structure as "FB" to distinguish it from the previously reported FBs.

As it turns out, there is a spectrum of solutions between the example found here and that reported in Refs. 25 and 26. The resulting compound structure can take on several forms

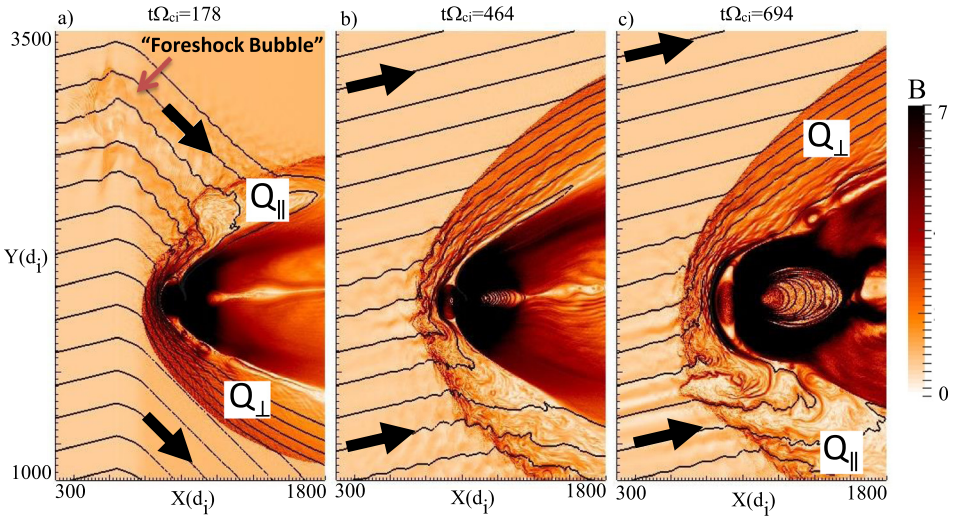

FIG. 1. (a)-(c) Time evolution of the magnetosphere in run 1 where the IMF direction changes in time. The arrows indicate the direction of the magnetic field. A large foreshock bubble is evident in panel (a). Details of this structure are shown in the next figure. The positions of the $Q_{\parallel}$ and $Q_{\perp}$ regions move due to the change in the IMF direction. Note the higher level of fluctuations associated with the $Q_{\parallel}$ magnetosheath. In panel (c), streaks of enhanced magnetic field are observed in the magnetosheath. These are associated with the formation of high velocity jet that penetrates deep into the magnetosheath.

depending on the thickness of the RD, the IMF direction, among others. Particularly important is the level of density depression in the cavity formed near the shockfront. The larger the density depression, the hotter the temperature within the cavity. In moderate density depressions such as those in Figure 2 ($> 0.1N_o$), the cavity does not increase in size significantly. Note, however, that the size of the shockfront here in both x and y directions can still reach several hundred ion inertial lengths as seen in Figure 2. For more extreme density depressions approaching $\sim 0.05N_o$, the shockfront and the cavity become one structure and can grow to very large scales even reaching the size of the magnetosphere if given sufficient time. However, one has to be cautious regarding simulations of such structures in the hybrid code. Standard hybrid codes are not ideally suited for treatment of structures when the density depression reaches

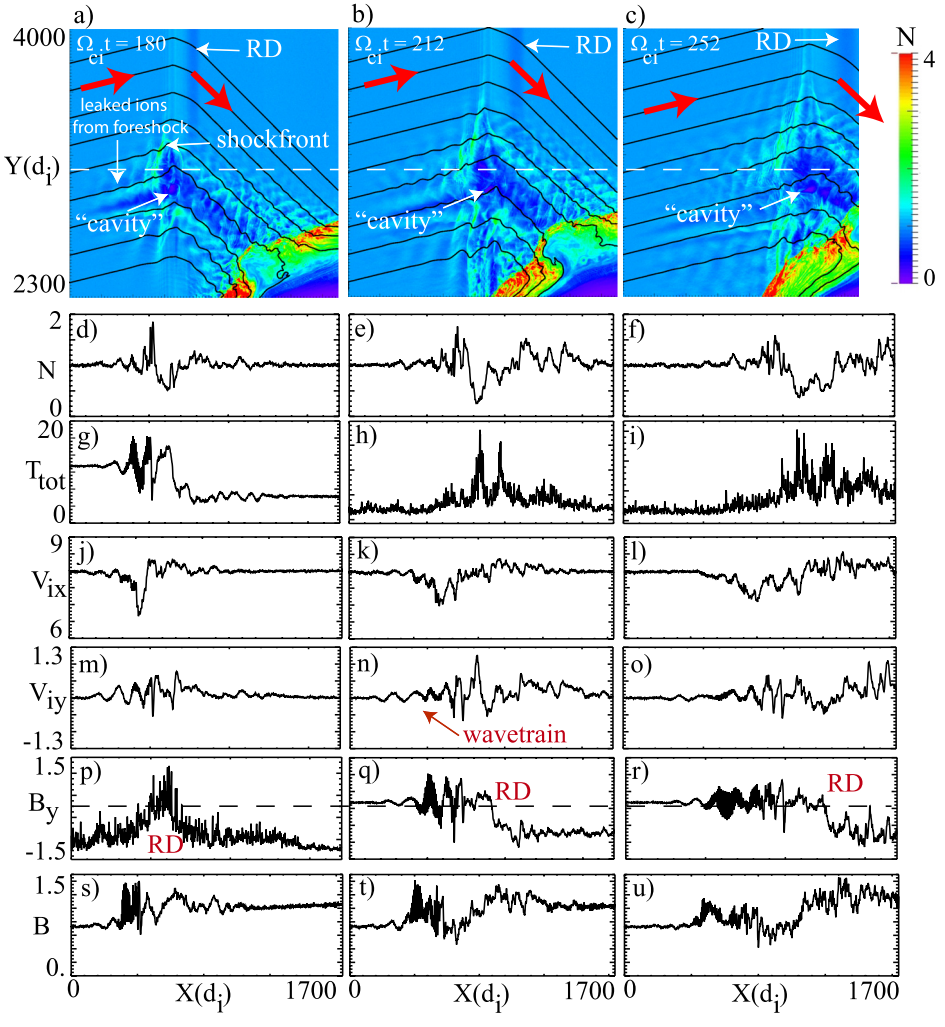

FIG. 2. Time evolution of the foreshock bubble in run 1 and 1D cuts of density, total ion temperature, the x and y components of ion velocity V_{ix}, V_{iy}, and the y-component and total magnetic field B_y, and B. The change in the IMF direction launches a RD which interacts with the ions reflected from the shock, giving rise to a shockfront and a density cavity in the solar wind. The red arrows indicate the direction of the magnetic field. Reflected ions in the foreshock penetrate through the shockfront, streaming along the new incoming IMF direction. Observational signature is sunward moving particles on field lines that do not point at the bow shock. The RD separates from the shockfront in time.

the density floor set in the simulations. And we have found a tendency to see weaker cavities with use of larger number of particles per cell and/or higher resolutions. We will examine the formation of foreshock bubble using fully kinetic simulations elsewhere. An observational signature of such a structure, assuming it can be realized in nature, would be a large region of the solar wind populated with very low density and hot plasma.

B. Characteristics of turbulence and its time evolution

As is evident from Figure 1(a), the quasi-parallel magnetosheath appears more turbulent than the quasi-perpendicular magnetosheath. And after the IMF change, the new quasi-parallel magnetosheath in Figures 1(a)–1(c) appears more turbulent than the new quasi-perpendicular magnetosheath. This is confirmed by calculation of the magnetic field fluctuations which are about a factor of 4 larger in the $Q_{\parallel}$ regions. This higher turbulence level is also confirmed by additional diagnostics in Figure 3. Figures 3(a) and 3(b) show the magnetic field spectrum and the kurtosis (fourth standardized moment) of magnetic field increments $\delta B(x,s) = B(x+s) - B(x)$ as a function of separation length s for the foreshock, $Q_{\parallel}$ and $Q_{\perp}$, magnetosheath respectively. Kurtosis, or flatness, is a measure of deviations from Gaussian. The flatness of Gaussian is exactly three. The $Q_{\parallel}$ magnetosheath shows clear turbulent features, i.e., an energy spectrum with close to $-5/3$ range and strong non-Gaussianity (i.e., a very large kurtosis which increases as the length scale decreases). Interestingly enough, the kurtosis values are in good agreement with in situ measurements of $Q_{\parallel}$ magnetosheath in cases where evidence of turbulent reconnection was reported.[13] In contrast, the kurtosis of the foreshock and the $Q_{\perp}$ magnetosheath are much smaller. In particular, the kurtosis of $Q_{\perp}$ is almost flat with values between 4 to 5, showing no or almost no signature of intermittency. Intermittency is a signature of the generation of coherent structures. As we will demonstrate shortly, turbulence generates coherent structures in the form of reconnecting current sheets and magnetic islands in the $Q_{\parallel}$ but not in the $Q_{\perp}$ magnetosheath, consistent with the kurtosis diagnostics. Figure 3(c) shows the comparison of the ion energy distribution function in the foreshock, $Q_{\parallel}$, and $Q_{\perp}$. The foreshock shows the presence of a counter streaming population as expected. The magnetosheath shows power-law distribution functions but with different power-law indices for the $Q_{\parallel}$ and the $Q_{\perp}$ cases. The thermal energy and the high energy particle production are significantly higher in the $Q_{\parallel}$ magnetosheath. This is not surprising since higher levels of turbulence in the $Q_{\parallel}$ region can lead to additional heating and acceleration of particles. Another mechanism for acceleration to high energies is the Fermi process which requires the particles to go back and forth across the shock several times. Since particles can move along the magnetic field more readily than across it, and because magnetic field lines move along the bow shock as the result of their advection with the solar wind, one might expect more energetic particles in the $Q_{\parallel}$ magnetosheath since field lines there have been connected to the bow shock the longest. The relative importance

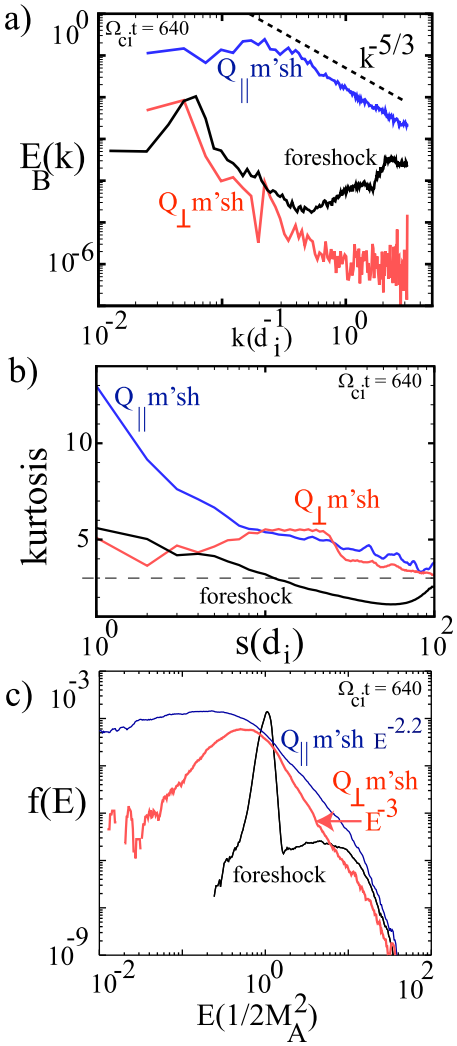

FIG. 3. Comparison of turbulence characteristics in the foreshock and the $Q_{\parallel}$ and the $Q_{\perp}$ magnetosheath at $\Omega_{ci} = 640$ for run 1 (Figure 1). (a) Omnidirectional energy spectra of magnetic field. Only $Q_{\parallel}$ magnetosheath shows a 5/3 power-law in this case. (b) Kurtosis, a measure of non-Gaussianity, of magnetic field increments $\delta B(x,s) = B(x+s) - B(x)$ as a function of the separation length s is shown. An increase in kurtosis at smaller scales is an indicator of the presence of coherent structures. Only the $Q_{\parallel}$ region shows this behavior in this run. (c) Ion distribution function versus energy normalized to upstream flow energy. Foreshock shows the presence of two counter streaming populations. Both the $Q_{\parallel}$ and $Q_{\perp}$ magnetosheath show power-laws. We have used the following range of x and y for each region in panels (a) and (b): for foreshock $x = [301 - 556d_i]$, $y = [1301 - 1812d_i]$, for $Q_{\parallel}$, $x = [681 - 808d_i]$, $y = [1651 - 1906d_i]$, and for $Q_{\perp}$ $x = [1401 - 1656]$, $y = [2801 - 3056d_i]$. In panel (c), we have binned the energy, measured in the simulation frame, into 500 logarithmically based segments and chosen the following range of x and y: for foreshock $x = [400 - 500d_i]$, $y = [1500 - 2000d_i]$, for $Q_{\parallel}$, $x = [700 - 800d_i]$, $y = [1500 - 2000d_i]$, and for $Q_{\perp}$ $x = [1500 - 1800d_i]$, $y = [2700 - 2900d_i]$.

between these competing processes is beyond the scope of the present work and will be explored elsewhere.

The power-law indices found here are not universal and can vary under different magnetosheath conditions. Previous 1D hybrid simulations of quasi-parallel shocks have also shown power-laws over a similar range[27,28] but they show flattening of the particle spectrum at higher energies where we do not have sufficient statistics. This flattening of the particle spectrum is also seen in 2D hybrid simulations of perpendicular shocks that include pre-existing, large-scale

magnetic-field turbulence in the upstream region.[29] The details of the turbulence are clearly very different in our simulations as compared to 1D simulations where reconnection and magnetic islands are excluded. Direct comparison of particle energization in local shock simulations versus our global simulations will be presented elsewhere.

In the present study, the initial solar wind ions are taken to have a Maxwellian distribution function. However, nonthermal ion distribution functions are commonly observed in the solar wind. The presence of nonthermals can affect the instabilities in the foreshock which in turn can affect the details of turbulence and associated particle energization. This is an important extension of the present work that we are currently working on.

Next, we compare the evolution of the turbulence level as measured by the root mean square of the magnetic field fluctuation amplitude $B_{rms} = \left(\sum_{i=1}^{n} (B_i - \langle B \rangle)^2 / n\right)^{1/2}$ which is normalized to B_o. Here, $\langle B \rangle$ is the average magnetic field in the region where B_{rms} is calculated. We use run 2 where the IMF direction remains at 10° during the entire length of the simulation. We have run the simulation to longer times than previous hybrid simulations so that we can explore the asymptotic behavior of the turbulence. The result is shown in Figure 4(a). Although the foreshock turbulence is a major source of turbulence downstream of the quasi-parallel shocks, the correlation between the turbulence level in these two regions is more complex as evident in Figure 4(a). While on average the increase or decrease in the foreshock activity leads to a corresponding increase or decrease in the turbulence levels downstream, there is a temporal lag between changes in the foreshock and its transmission to magnetosheath. For example, there is no discernible increase in the foreshock turbulence levels from time of 200 to 500, whereas the $Q_{\|}$ turbulence level has increased by a factor of nearly 2.4. However, in time the foreshock turbulence level starts to drop off, and the turbulence level downstream of the shock also starts to decrease.

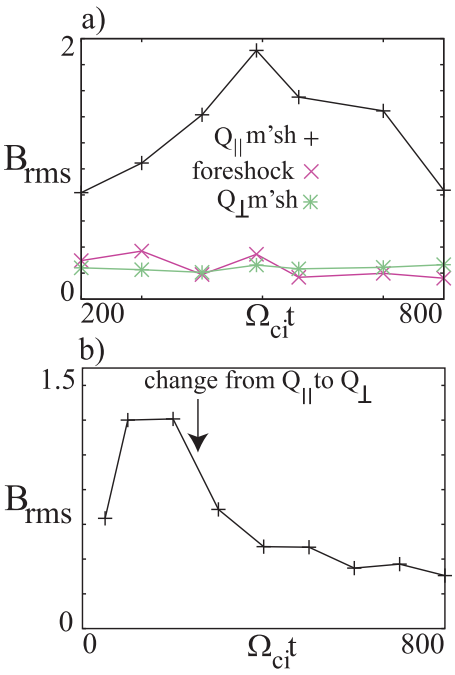

FIG. 4. Time evolution of turbulence fluctuation levels as measured by B_{rms} which is normalized to B_o. (a) As the magnetosphere forms (run 2), ions start to get reflected from the $Q_{\|}$ segment of the bow shock. This in turn drives the upstream turbulence as evident in an initial rise in B_{rms} until it reaches a peak of nearly 2. After the peak, B_{rms} starts to weaken as the foreshock B_{rms} also weakens. B_{rms} in the $Q_{\perp}$ is driven by the temperature anisotropy and is more steady in time. The higher B_{rms} in $Q_{\|}$ as compared to the foreshock is not surprising since the turbulence convected from upstream through the shock gets amplified in the process. (b) In run 3, the IMF direction changes in time, resulting in the switch of the geometry of an originally $Q_{\|}$ to $Q_{\perp}$. This switch is shown to lead to rather rapid drop in B_{rms} and it settles down to B_{rms} levels similar to those in the $Q_{\perp}$ in panel (a).

As another way to see this, and also to get a handle on the timescale for decay of turbulence levels once the geometry changes from quasi-parallel to quasi-perpendicular (Fig. 4(b)), we examine time evolution of B_{rms} for run 3. This run, which is a higher resolution ($0.5d_i$) version of run 1, has identical parameters as run 2 except that the IMF direction is changed from −45° to 10° after $\Omega_{ci}t = 90$. We used this run as part of our convergence study to ensure the results are not affected by cell resolution or number of particles. It is seen that the change to quasi-perpendicular geometry results in a rapid drop in the turbulence fluctuation levels to about $B_{rms} \sim 0.3$ which is similar to that in the $Q_{\perp}$ magnetosheath in Figure 4(a). It is interesting to note that the mean rate of solar wind IMF directional discontinuities is about 0.5−2.5 h (Ref. 30) or about $\Omega_{ci}t \sim 150 - 750$. This is competitive with decay times of turbulence in the magnetosheath and provides a natural low frequency "stirring" mechanism for the magnetosheath turbulence.

The significantly enhanced level of turbulence in the $Q_{\|}$ magnetosheath has implications for the nature of turbulence as we now demonstrate.

C. Reconnection in the magnetosheath

In 2D, the presence of magnetic islands formed through reconnection can be demonstrated by plotting the contours of the out-of-the-plane vector potential or tracing of magnetic field lines. An effective way to visualize field lines is through the line-integral-convolution (LIC) technique (see the Appendix) which we first introduced in plasma physics in our study of shear driven turbulence.[3] Figure 5 shows the magnetic field lines colored by V_x for a zoomed in area of the quasi-parallel shock for run 1 at $\Omega_{ci} = 694$. The magnetic field intensity plot of a larger region of this simulation was shown in Figure 1(c). Figure 5 clearly shows a wide range of magnetic islands up to $\sim 30d_i$ in diameter. Some of the islands show evidence of outflowing jets (not shown).

These magnetic islands are observed in the quasi-parallel but not in the quasi-perpendicular magnetosheath (not shown). The absence of magnetic islands in the $Q_{\perp}$ magnetosheath is the reason for differences in the kurtosis in the $Q_{\|}$ and $Q_{\perp}$ regions shown earlier (Fig. 3(b)). Also note that the islands can exist even in the vicinity of the $Q_{\|}$ region of the bow shock. Due to the small size of these magnetic islands/flux ropes, they are not expected to be force free.

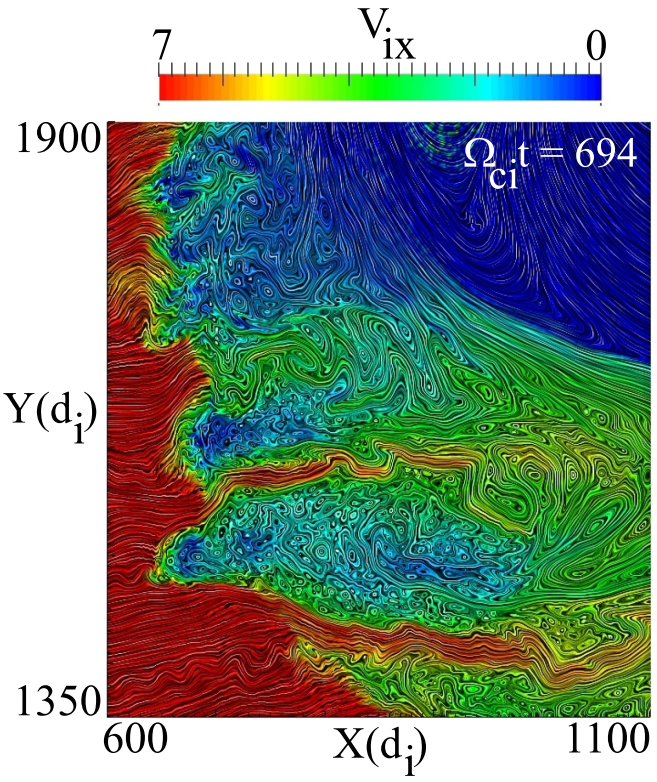

FIG. 5. Formation of a hierarchy of magnetic islands due to $Q_{\|}$ magnetosheath turbulence in a global hybrid (run 1) simulation. This is a zoomed view of the $Q_{\|}$ region of Figure 1(c). Here, the LIC technique is used to visualize the magnetic field lines. The LIC is colored by V_{ix}. In addition to the magnetic islands, the presence of at least two jets inside the magnetosheath having velocities comparable to the solar wind speed is evident (red streaks in the magnetosheath).

These results are consistent with Cluster observations of magnetosheath reconnection events[12,13] which also were only present in the quasi-parallel magnetosheath. Although postulated, no search for mangetic islands was conducted in these observational studies. Detection of small magnetic islands is challenging but given that some of the islands grow to as large as $\sim 30-40d_i$, it may be possible to find such islands in the data.

We have found the reconnecting current sheets and magnetic islands to be a common feature of quasi-parallel shocks. Since the size of the magnetosheath is larger for larger D_p, the number of islands and their interactions increases at larger D_p. Figure 6 shows the density and the LIC of magnetic field colored by the strength of B for run 4 ($D_p = 300$). The magnetosheath is found to be almost completely volume filled with magnetic islands in this case.

D. Enhanced heating of $Q_{\|}$ magnetosheath

The enhanced turbulence level in $Q_{\|}$ magnetosheath also leads to stronger heating as compared to $Q_{\perp}$ magnetosheath as evident in Figure 7. We have found evidence for this in the observations. Figure 8 shows the statistical map of THEMIS measurements between October 2007 and October 2013 when the probes occupied the magnetosheath. The quantity binned here is the mean value of the total ion temperatures during a Parker-Spiral IMF ($B_x > 0.2|B|$ and $B_y < 0.2|B|$ or $B_x < 0.2|B|$ and $B_y > 0.2|B|$), which is presented in the Magnetosheath InterPlanetary Medium (MIPM) reference frame. The MIPM frame uses upstream measurements to arrange within a normalised model magnetosheath thus accounting for boundary motion and planetary aberration. For a detailed description of the MIPM frame and subsequent data processing, we refer the reader to access the methodology paper which also compares the statistical mapping results against global MHD simulations produced by the CCMC BATS-R-US code.[31] To briefly summarize, the MIPM frame arranges points as a function of the upstream IMF. Therefore, statistically it can be closely compared to an aberrated GSE system during parker-spiral IMF orientation where $Y_{MIPM} > 0$ represents a quasi-perpendicular shock and $Y_{MIPM} < 0$ quasi-parallel. The physical dimension of each bin is 0.5×0.5 Earth radii and the bin number density is typically a hundred data points per bin. Each data point is calculated from the mean averaged 3-min intervals of THEMIS data. Currently, the data are binned using a 20 min sliding averaged OMNI data around each 3 min THEMIS data interval. The points during which IMF cone angle varies more than 20° are removed. It is clear that the dayside MSH is hotter due to the shock compression and the hot plasma region extends more tail-ward at the quasi-parallel shock side of the magnetosheath, possibly due to kinetic processes. The quantitative calculation as a function of MIPM-frame zenith angle shows that the magnetosheath downstream of the quasi-parallel bow shock is on average about 10%–15% hotter. A more detailed temperature study using THEMIS data for various solar wind conditions and quantitative comparisons between dawn and dusk sectors will be discussed elsewhere.

E. Global fully kinetic simulation

Hybrid codes do not include electron kinetic effects. As such, magnetic reconnection in hybrid simulations occurs due to either numerical or imposed resistivity. To confirm that the magnetosheath reconnection events observed in our hybrid simulations are not due to numerical effects, we have also conducted a 2D global fully kinetic simulation for the radial IMF condition. The detailed comparison of this run with an equivalent hybrid simulation will be presented elsewhere. Here, our interest is only to establish that reconnection and magnetic islands also occur in the global fully kinetic simulation.

The simulation was performed using a general-purpose plasma simulation code VPIC.[32] The simulation is of size $2000 \times 1500d_i$ with $56{,}544 \times 41{,}984$ cells. The IMF magnetic field is in the x direction and the dipole is oriented at an angle of 80° with respect to the IMF. The incoming solar wind plasma has parameters $M_A = 8$, $T_i = T_e$, $\beta = 8\pi(T_e + T_i)n_o/B_o^2 = 1$, $\omega_{pe}/\omega_{ce} = 3$. The solar wind is normal to the dipole. The ion-to-electron mass ratio is $m_i/m_e = 50$. The strength of the dipole corresponds to stand-off distance $D_p = 50d_i$. Reflecting boundary conditions for particles are prescribed on a circle of radius $R = 0.3\ D_p$ around the geometrical center of the dipole. The dipole is created by prescribing out-of-plane current in two circular regions of the simulation domain or radius $0.1R$ separated by distance

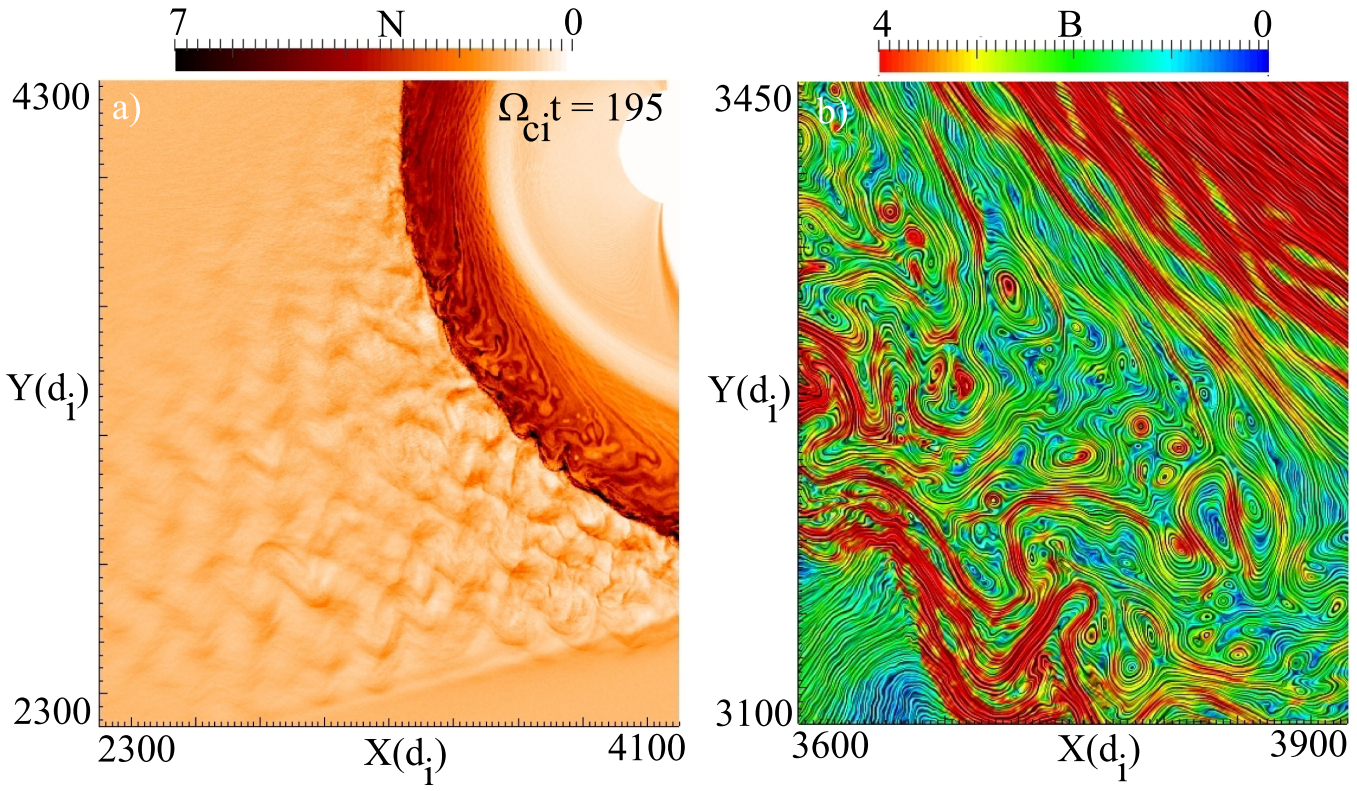

FIG. 6. Formation of turbulence and associated magnetic islands for a run with $D_p = 300$ (run 4). We have examined the properties of turbulence for a range of parameters, including different dipole field strength. The formation of the magnetic islands seems to be a common feature of $Q_{\parallel}$ magnetosheath turbulence in regimes where $B_{rms} \sim 1$. (a) Intensity plot of density. Only a segment of the simulation is shown. The presence of upstream waves is clearly evident. In the magnetosheath, current sheets and magnetic island can also been seen. (b) A close up of $Q_{\parallel}$ magnetosheath using LIC to show magnetic field lines colored by B. Many magnetic islands are observed at the shock surface all the way to the vicinity of the magnetopause.

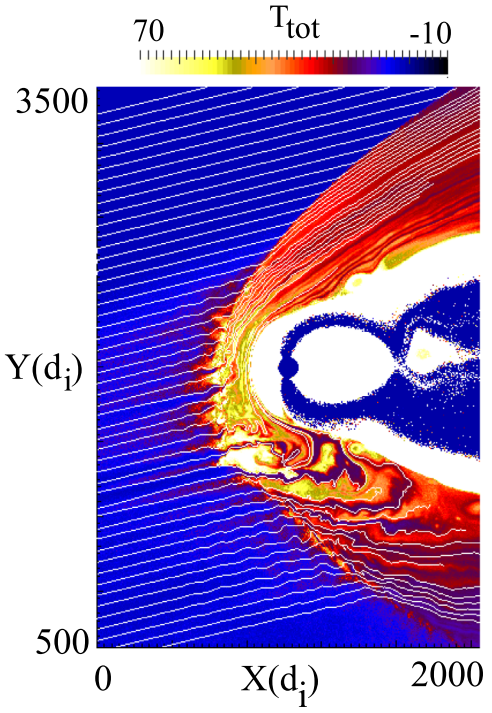

FIG. 7. Plot of the total ion temperature for run 1 at $\Omega_{ci}t = 694$. Magnetic field lines are overlaid in white. The enhanced magnetosheath heating in the $Q_{\parallel}$ as compared to $Q_{\perp}$ magnetosheath is clearly evident. Although temperature is a positive quantity, the range of color bar is only to improve the contrast in the figure.

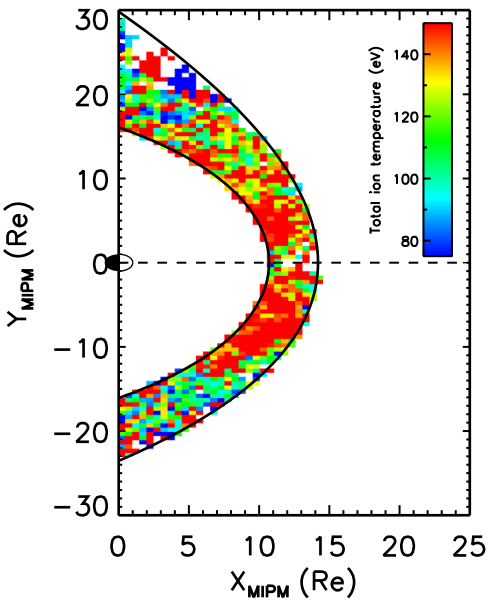

FIG. 8. THEMIS measurements between October 2007 and October 2013 of the mean value of the total ion temperatures in the magnetosheath during a Parker-Spiral IMF in the MIPM reference frame. The physical dimension of each bin is $0.5 \times 0.5 R_E$ and the bin number density is typically a hundred data points per bin. Each data point is calculated from the mean averaged 3-minute intervals of THEMIS data. The MSH downstream the quasi-parallel bow shock region is about 10%–15% hotter.

0.25R. The initial conditions correspond to a uniform plasma with solar wind parameters. In order to minimize the perturbations created by the initial conditions, the strength of the currents creating the dipole is ramped up in time as $j = j_0[1 - \exp(-t/\tau)]$, where $\tau = 30\Omega_{ci}^{-1}$.

The result is illustrated in Figure 9 where only a segment of the simulation around the quasi-parallel region is shown. The LIC of magnetic field is shown colored by ion density. As in the hybrid example, many magnetic islands are observed in the quasi-parallel magnetosheath. Our closer examination of the magnetic field structures (not shown) shows the hierarchy of islands extending down to the electron kinetic scales. However, the largest islands have similar size ($\sim 30d_i$) as in the hybrid simulations.

IV. TRANSMISSION OF THE FORESHOCK TURBULENCE

It is well known that the relative streaming of ions reflected from the bow shock and the incoming solar wind leads to the generation of large amplitude ultralow frequency (ULF) waves.[6] As these waves get convected back towards the shock, they can steepen, giving rise to shocklets and SLAMS. Here, we examine the evolution of such structures, their interaction with the bow shock, and their role in magnetosheath turbulence. For simplicity, here we refer to the steepened structures as wavefronts or shocklets. As seen from Figure 10, the wavefront-magnetosphere interaction

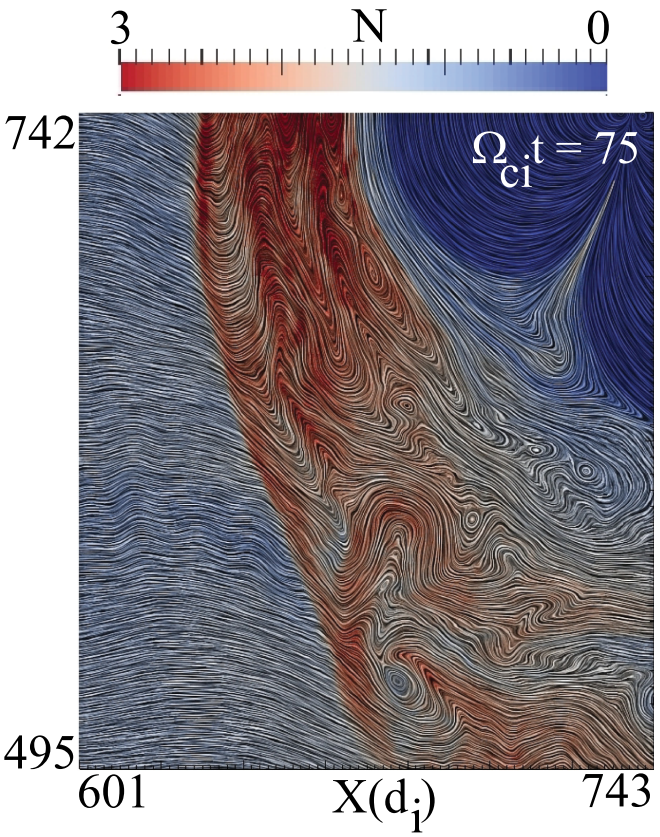

FIG. 9. Formation of a hierarchy of magnetic islands due to $Q_{\|}$ magnetosheath turbulence in a global fully kinetic simulation for radial IMF conditions. Only a zoomed in view of the $Q_{\|}$ region is shown. The LIC of magnetic field is colored by density.

falls into four stages. The IMF is nearly radial in this case (run 5). The part of the wavefront hitting the bow shock first gets compressed to shorter scales (Figs. 10(a), 10(c), and 10(d)), causes a rippling of the shockfront as well as local spike in the temperature (Fig. 10(b)). As the wavefront gets through the shock (Fig. 10(e)), its amplitude is amplified (Fig. 10(g)). The waves persist as wavefronts in the magnetosheath for tens of ion cyclotron times (Figs. 10(i)–10(l)) but then they start to break up and dissipate their energy. In this way, turbulence upstream gets amplified and contributes to the turbulence in the magnetosheath.

Interestingly enough, large amplitude waves have also been observed downstream of the quasi-parallel shocks at Venus. A recent study compared detailed wave diagnostics in both upstream and downstream regions of the Venusian bow shock and concluded that the downstream waves are transmitted ULF waves.[33]

In cases where the steepened fronts are nearly parallel to the quasi-parallel region of the bow shock surface, they can significantly modify the shock structure and the magnetosheath thickness. This is shown in Fig. 11, from run 6, which shows the time evolution of density and B_y. The propagation of one wavefront, labeled as WF1, is marked in time. The steepened front is evident in Figures 11(a) and 11(e). Note that the steepened front has many properties similar to a shock, exhibiting localized density and magnetic pulses/enhancements over the background values. By the time $\Omega_{ci}t = 47.2$, the front has gained strength (Figures 11(b) and 11(f)) and creates a large density jump ahead of the shock (Figure 11(b)). The thickness of the magnetosheath is much thinner in this region as compared to the upper region away from the shocklets. A rather large magnetic island of about $10d_i$ in width is evident as a circular loop in the density panels. WF1 grows in scale (Figures 11(c) and 11(g)) and eventually gets convected into the shock and moved downstream (Figures 11(d) and 11(h)). This process can repeat for several cycles. This is evident in Figures 11(d) and 11(h) which show the formation of a second wavefront (WF2) which will go through the same process as WF1. Figure 12 shows a blow up of B_y and an associated 1D cut across the wavefront at $\Omega_{ci}t = 47.2$. The 1D cut shows the amplification of the wavefront amplitude as it crosses the shock into the magnetosheath.

Figures 13(a) and 13(b) illustrate the dynamics between the shocklet and the bow shock. The LIC of magnetic field colored by density and LIC of ion velocity colored by V_x are shown for a zoomed in region of Figure 11(c). The shocklet presents an obstacle to the flow, generating local spikes in the density (Fig. 13(a)) and the magnetic field, and decelerating the flow (Fig. 13(b)). The region between the shocklet and the magnetosheath can be quite turbulent. Several vortices and magnetic islands are clearly evident in this in-between region, similar to the magnetosheath. Note also the presence of a relatively large magnetic island spanning about $10d_i$ along the magnetopause surface. The vortices are apparent here since the flow speed is nearly zero in the shown regions. The crossing of such shocklet/bow shock structures may be mistaken as multiple shock crossings in the data, especially since there are regions with conditions similar to the solar wind in between them.

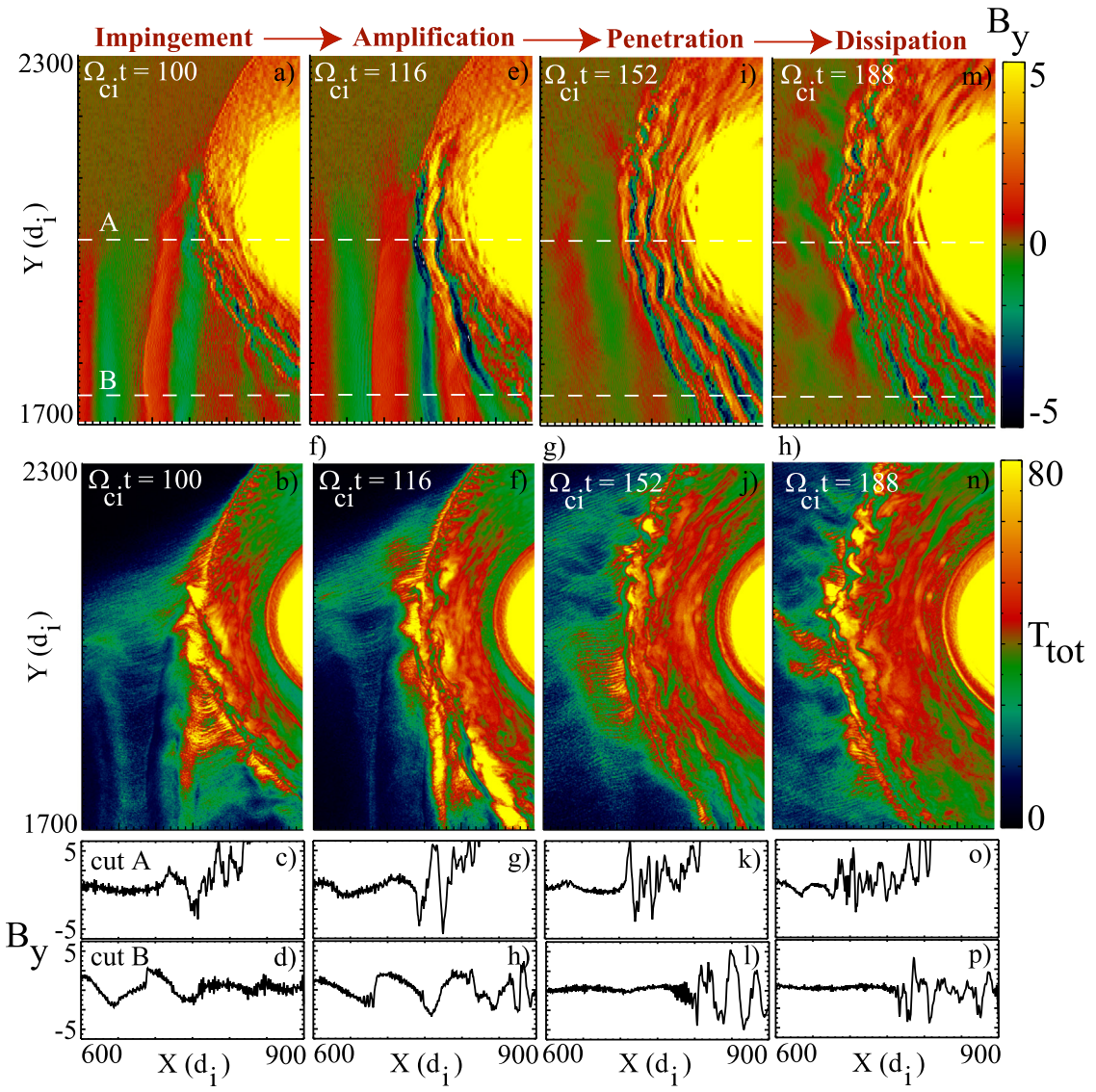

FIG. 10. The interaction of upstream wavefronts with the bow shock (run 5) is shown to consist of four stages. The waves are formed due to the relative streaming of shock reflected ions and the incoming solar wind. Due to the high solar wind speed, the waves get convected back towards the bow shock. Some of the waves steepen prior to hitting the shock (panels (a)–(d)). As the wavefronts go through the shock, they get amplified and compressed to shorter wavelengths (panels (e)–(h)). The presence of a coherent series of wavefronts inside the magnetosheath is evident in panels (i)–(l). After some time, however, the wave structures get dissipated and are disrupted (panels (m)–(p)). Thus shortly after a radial IMF turning, coherent wavefronts should be observable in the magnetosheath, but at later times, only turbulence would be observed.

Another effect of ion foreshock that is perhaps not widely appreciated is that it reduces the magnetosonic Mach number as evident from the 1D cut in Figure 14. As such, the ion foreshock helps in the shock dissipation process and affecting the slowing of the plasma. The presence of the jets can also been as streaks of high magnetosonic Mach number within the magnetosheath (Figure 14). The modification of M_s due to the ion foreshock is consistent with an observational study where significant evolution of interplanetary shock parameters was observed during its motion along the bow shock.[34]

V. ANOMALOUS FLOWS

In this section, we demonstrate the effects of turbulence on the magnetosheath flow. There are a number of diagnostics that are useful for visualizing flow. These include streamlines, pathlines, and streaklines. Streamlines represent instantaneous patterns of the flow. A true vortical pattern on scales larger than kinetic scales would wrap the magnetic field. However, the presence of such a vortex can be masked, using streamlines, in the presence of a large background flow as is the case in the magnetosheath. Instead, we use streaklines to study the mechanisms for formation of sunward flow and vortices in the magnetosheath. Streaklines provide a time history of the flow and can reveal the presence of vortical pattern even in case of large background flow. Each streakline is created by tagging and following the trace of fluid elements passing through a particular spatial point. Streaklines can be thought of the pattern traced by dye if one were to steadily inject dye into the fluid at a fixed point.

A. High speed jets

An interesting feature evident in Figure 5 is the presence of two ion jets, shown as red, that penetrate deep inside the

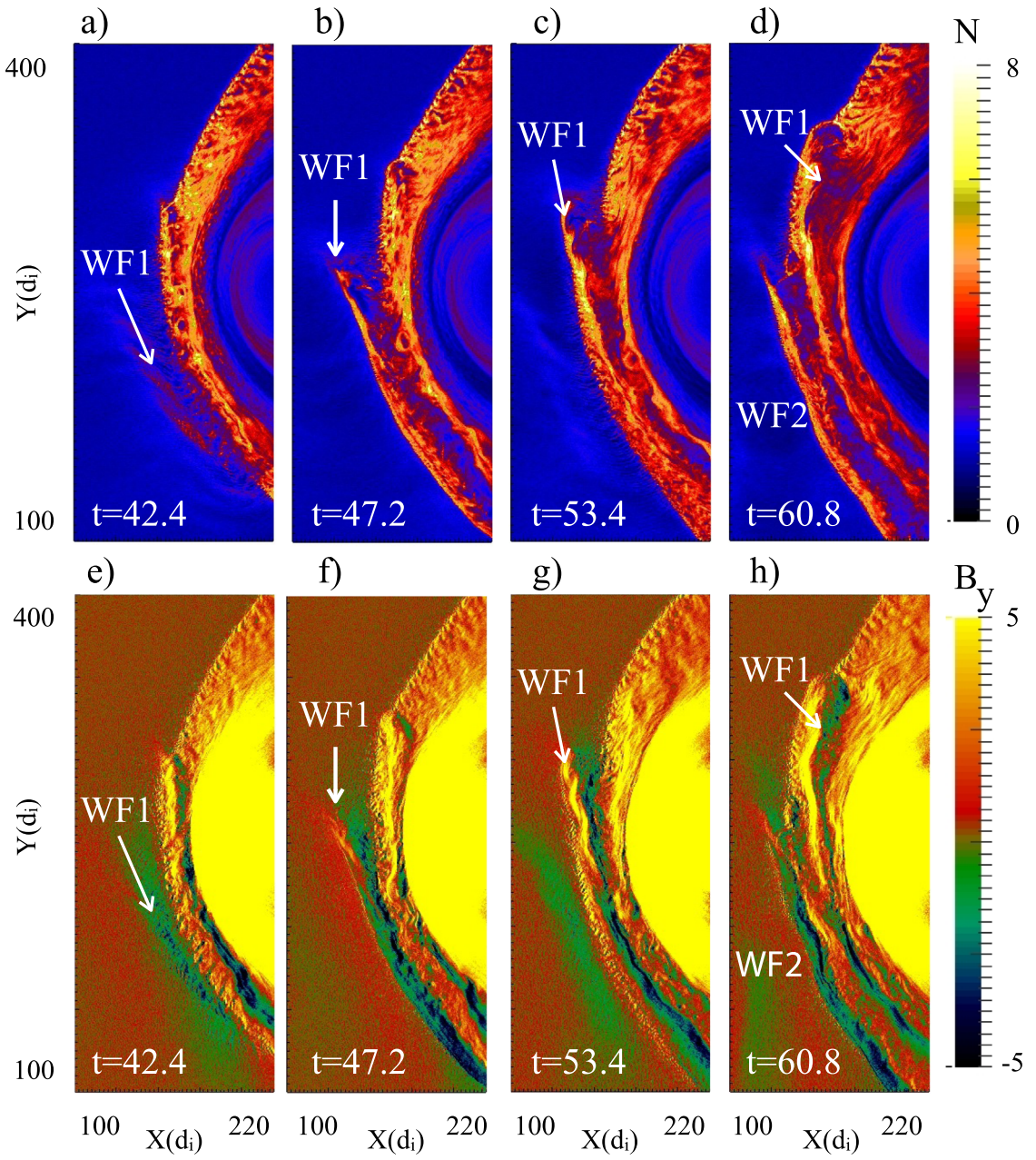

FIG. 11. In cases where the steepened wavefronts become nearly parallel to the $Q_{\|}$ segment of the bow shock, they can significantly modify the bow shock and the size of the magnetosheath. The process stages of evolution starting from impingement to eventual dissipation of the wavefronts indicated in Figure 10 also occur here as indicated by tracking of one wavefront labeled as WF1. Note the formation of a second wavefront, WF2, in panels d and h, that will repeat the process.

magnetosheath. The magnetic field lines are seen to remain nearly radial as in the solar wind along these jets, embedded in an otherwise sea of magnetic islands. In this section, we examine these jets in more detail. Figure 15 shows plots of the dynamical pressure over a larger region of the simulation than in Figure 5. Presence of many jets is evident, seen as streaks of high dynamical pressure, with some reaching the magnetopause. As the jets slow down in the magnetosheath, they form a bow wave (Fig. 15) which can be as large as several hundred d_i. The interaction of the jets/bow wave with the magnetopause causes strong perturbations, giving rise to surface waves, and/or inner-magnetospheric compressional waves.[11,35,36] And in this case, this interaction has triggered flux transfer events (Fig. 15(b)), although the IMF is 10°. The jets also lead to significant inhomogeneities in the magnetosheath and serve as an additional driver of turbulence. Figure 15(b) shows the LIC of B for an area zoomed in around the large bow wave in Fig. 15(a). This leads to another source of reconnection and generation of magnetic islands in the magnetosheath.

In time, the jets get convected towards the tail while new jets are formed. Figure 16 shows the properties of the jets, which strongly deviate from the surrounding magnetosheath. In particular, jets exhibit enhanced magnetic field strength (Fig. 16(b)), lower temperature (Fig. 16(c)), and higher density (Fig. 16(d)) than the surrounding magnetosheath. Note also the strong kinking of the magnetic field (Fig. 16(b)) along the jets. In each case, we have found the

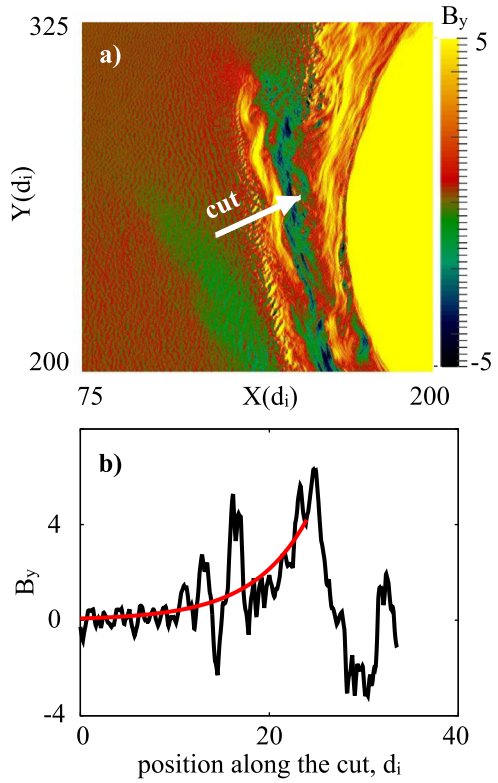

FIG. 12. Wave amplification across the shock. A zoomed in view of Figure 11(g) is shown in panel (a). A 1D plot of B_y along a cut in panel (a) is shown in panel (b). Note how the upstream wave is amplified as it crosses the bow shock. As a reference, the red curve shows an exponential curve through the B_y profile.

wavelength of the kinked jet to be in good agreement with the wavelength of Kelvin-Helmholtz instability based on local measurements of velocity shear and the thickness of the shear layer.

Observations have revealed the presence of transient enhancements of plasma flow within the magnetosheath characterized by various measures such as high dynamic pressure and kinetic energy density.[9,10,35,37–40] Hietala *et al.*[9] reported high velocity jets during nearly radial conditions (IMF angle less than 20°) for $M_A = 12$. They found the plasma density to be compressed along the jets with density depletions around them, the velocity of the jets to be close to the upstream value, and the width of them on the order of 50 to 100 ion d_i. These features are fully consistent with the observed jets here. The velocities of the jets shown in Figure 5 are close to the solar wind speed of $8V_A$, their widths are in the range of 20 – $60d_i$, and there is density compression on the order of a factor of 6 along the jets (Fig. 16(d)) and large density depletions around them, with densities dropping below the solar wind density in some cases. The size and the level of the depletion area vary on time. The ion temperature (Fig. 16(c)) shows that the temperature does not change significantly along the jets. This is also consistent with properties of the observed jets.[9,10] This may also explain previous observations[41] which had found cases where the solar wind passes through the shock layer without significant heating.

The origin of these jets has been controversial. Hietala *et al.*[9] attributed their formation to ripples along the shock surface. Since the shock mainly decelerates the component of the upstream velocity parallel to the shock normal, ripples along the shock cause local changes to the angle between these two vectors. For large angles, the shock speed would remain close to its upstream value. While others have suggested the origin of the jets to be due to interaction of the magnetosphere with solar wind discontinuities (e.g., Ref. 42) and others (e.g., Ref. 39) questioned the ripple-based mechanism. In contrast, a more recent study[10] using 4 years of subsolar magnetosheath observations concluded that 97% of the observed jets are consistent with the ripple idea. This finding is consistent with our simulation results where we find the bow shock surface to be highly rippled due to foreshock turbulence, and we find the jets even in cases where we keep the IMF direction fixed in time and there are no solar wind discontinuities.

B. Sunward flows

In the absence of turbulence, the downstream flow must be directed away from the bow shock at all points as seen in global MHD simulations. However, THEMIS observations during radial IMF conditions have shown evidence of sunward flows. Such flows are also seen in our simulations. Figure 17 shows V_{ix} for the same time in the simulation as in Figure 16. The purple areas are regions in the magnetosheath with negative V_{ix} with peaks around $2V_A$. Note that there are several regions along the bow shock where such sunward flows are present.

Several different mechanisms have been proposed to explain this anomalous flow. Shue *et al.*[11] attributed the origin of the sunward flow to the interaction of a fast anti-sunward flow of unknown origin with the magnetopause, which in turn causes the magnetopause to rebound, creating a sunward motion. As shown in Figure 16, the generation of fast anti-sunward flow is due to the rippling of the bow shock. Although some of the jets interact with the magnetopause, many terminate at significant differences away from the magnetopause (e.g., Figure 16(a)) and yet there are sunward flows in the vicinity of such jets (Fig. 17). This indicates that alternative mechanisms must be in play for the generation of sunward flow than that proposed by Shue *et al.*[11] The simulations enable us to study the generation mechanism of sunward flow in much more detail than is possible in spacecraft measurements.

We have seen that the jets snake around the highly inhomogeneous magnetosheath, some reaching the magnetopause while others are terminated earlier. As we will see, some of the jets encounter local magnetic field that is nearly perpendicular to them. This causes them to get deflected since it is difficult for plasma to traverse perpendicular to the magnetic field. This complex dynamics has a direct bearing on the formation of sunward flow. We use streaklines to follow the evolution of the flow. First, we examined the role of jets that reach the magnetopause in causing the sunward flow. Figure 18(a) shows the streaklines shortly after they were seeded in two regions in the foreshock. These two groups of seeds were carefully selected so as to follow both the plasma motion inside the two large jets that reach the magnetopause (painted in white) as well as the plasma motion around the

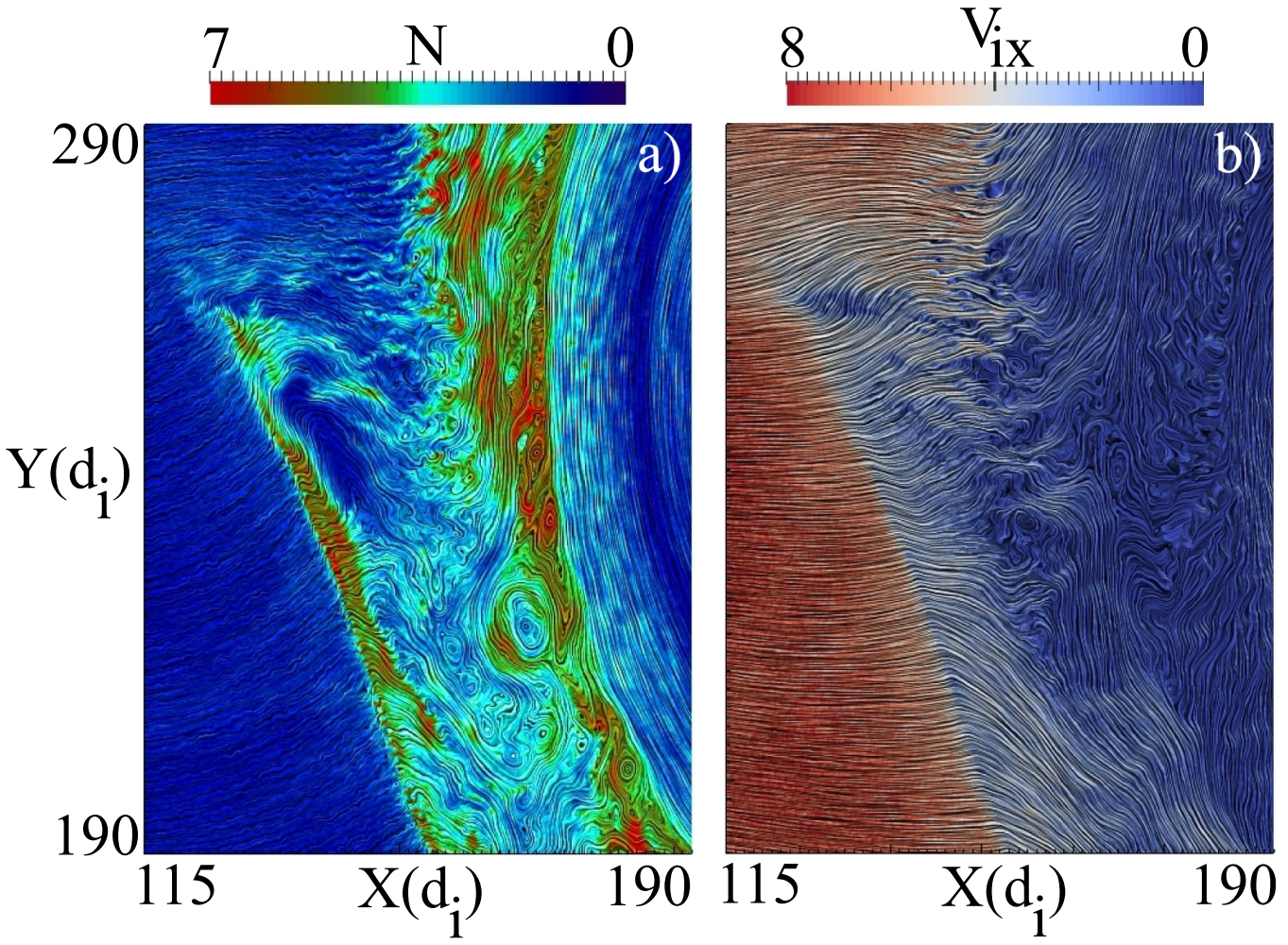

FIG. 13. Properties of the region in-between the shocklet and the bow shock. Close up of a shocklet in Figure 11(b) is shown. a) LIC of B colored by density. The shocklet has many properties similar to a fast shock, showing an increase in density and magnetic field within it. Note the formation of magnetic islands in the region between the shocklet and the bow shock as well as along the surface of the magnetopause. (b) LIC of ion flow colored by V_{ix}. Shocklet reduces the incoming flow speed and deflects it. An observational signature is the prediction of a turbulent solar wind density region upstream from the bow shock with almost no flow speed. A careful examination of this figure reveals presence of small scale flow vortices.

jets and their bow waves (painted in blue). Several points are immediately clear in Figure 18. First, the sunward flow is not caused by reflection of the jets. Second, there is no evidence that magnetopause motion is creating a large scale sunward flow. Third, in Figure 18(d), one of the largest jets has started to wrap although it has not formed a complete vortex. Any wrapping clearly created a sunward flow locally. Fourth, it is evident in Figures 18(b)–18(d) that the large bow wave pushes on the plasma around it, seen as blue streaks, as it propagates downward. This is another way that sunward flows can be generated.

Next, we seeded the field lines to examine the origin of the sunward flows between the jets that extend into the solar wind as were seen in Figure 17. The evolution of the streaklines is shown in Figure 19. Here again we marked the seeds in two colors, those that interact with the two jets marked as J_1 and J_2, marked in white and those that are from the areas in the vicinity but outside of these jets, marked in blue. The streaklines at the mouth of the opening in the region between J_1 and J_2 are seen to bend sunward as the blue streaklines penetrate this area (Figs. 19(c)–19(f)). The blue streaklines represent plasma that was pushed downward due to the pressure of the jets on the ambient plasma. In this way, the jet energy causes deflection of the ambient sunward, rather than the plasma within the jets being deflected.

As another check on the formation mechanism of sunward flow, we show in Figure 20 a zoomed-in view of the region containing jets marked as J_1 and J_2 in Figures 19(d) and 19(e). The top two panels show the LIC of magnetic field colored by ion temperature. The jets are seen to have a temperature similar to the solar wind whereas the area between the jets, marked as $R2$, is much hotter. The magnetic field lines clearly show that the surface of the bow shock is highly corrugated. A few sample magnetic field lines are plotted in white, while density contours are plotted in black. Note the presence of a band of nearly laminar magnetic field that is nearly perpendicular to the jets as they enter the magnetosheath, marked as $R1$. As the nearly parallel propagating jets encounter this band of magnetic field, they cannot penetrate further into the magnetosheath as it is difficult for plasma to move across the magnetic field. The upper jet is seen to snake around in the magnetosheath and gets deflected when reaching this band of magnetic field. The lower jet also winds around but does not cross this band of magnetic field. The plasma in the region between the two jets $R1$ gets squeezed

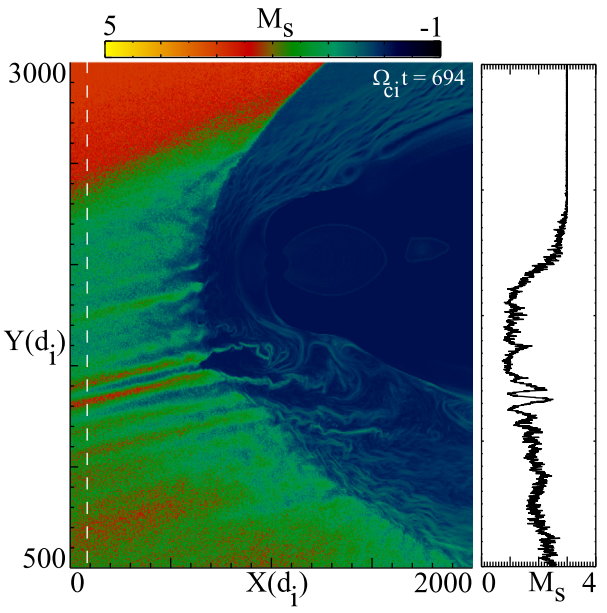

FIG. 14. Plot of the magnetosonic Mach number M_s for run 1. The reflected ions in the foreshock act to significantly lower the M_s upstream of the shock. Note the high M_s region in the magnetosheath, indicating the location of the jets seen in Figure 7.

and follows the magnetic field lines downward. This plasma pushes outward the shocked solar wind between the two jets in region $R2$, causing sunward flow as evident from negative V_{ix} flows seen in Figures 20(c) and 20(d). This picture is consistent with the development of the flow seen in Figure 19. The blue streaklines in Figure 19 represent the flow that follows the band of magnetic field lines $R1$ and enters the region between the two jets $R2$, creating sunward flow.

These considerations have led us to the following picture for formation of sunward flows. The jets, which have high dynamical pressure, "stir" the magnetosheath, creating large scale disturbances and pushing the ambient lower density plasma and the embedded magnetic field. The plasma in the sunward flow regions is not the plasma in the jets that was deflected, rather it is the plasma that was already there that is accelerated by thermal and dynamical pressure that develops because of the jets. In other words, the energy of the jets is deflected into sunward flow rather than the deflection of the jets themselves. This energy deflection can give rise to sunward flow that extends tens and even hundreds of ion inertial length into the solar wind, well past the nominal position of the bow shock (Fig. 17).

C. Large scale vortices

The presence of jets and sunward flows in the $Q_{\parallel}$ magnetosheath can drive velocity shears which can lead to formation of large vortices. Figure 21 (run 7) shows the formation of a large scale vortex which occurs in two stages. A structure akin to the Rayleigh-Taylor finger is formed (Fig. 21(a)) which then gets caught into the velocity shear in the magnetosheath (Fig. 21(b)), forming a large scale vortex (20c). The magnetic field lines are wrapped around, similar to a vortex generated by Kelvin-Helmholtz (KH) instability. Figure 22 illustrates the generation mechanism of the vortex using streaklines. A band of streaklines above the nominal stagnation line flow is seen to get deflected sharply and turn downward (pink) (Fig. 22(a)). This is due to the deflection of the energy of a jet which pushes the ambient plasma downward (not shown) similar to that for run 1 in Figure 19.

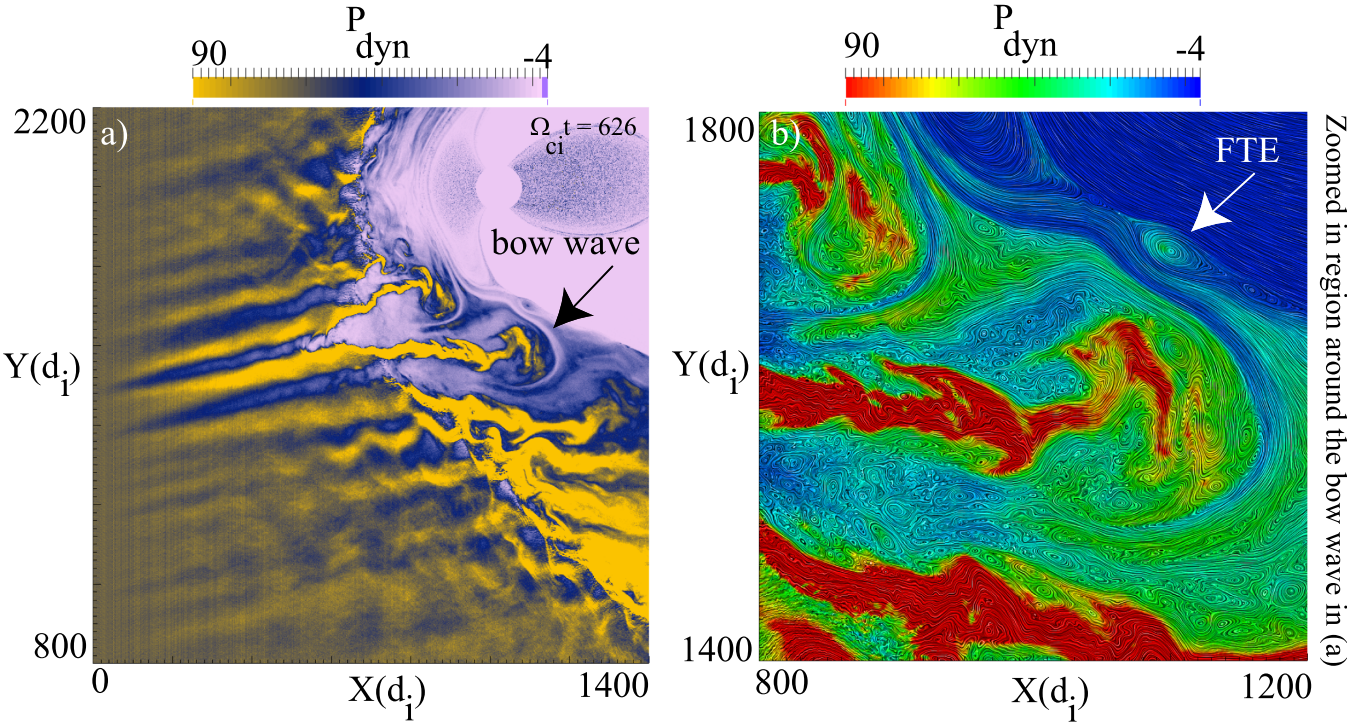

FIG. 15. Generation of jets inside the magnetosheath (run 1). (a) Plot of dynamical pressure in an area of the simulation zoomed in around the quasi-parallel bow shock. Some of the jets reach the magnetopause while others terminate closer to the bow shock. (b) LIC of magnetic field colored by dynamical pressure for an area zoomed in around a strong jet marked by the bow wave in panel "a" that has triggered a flux transfer event at the magnetopause.

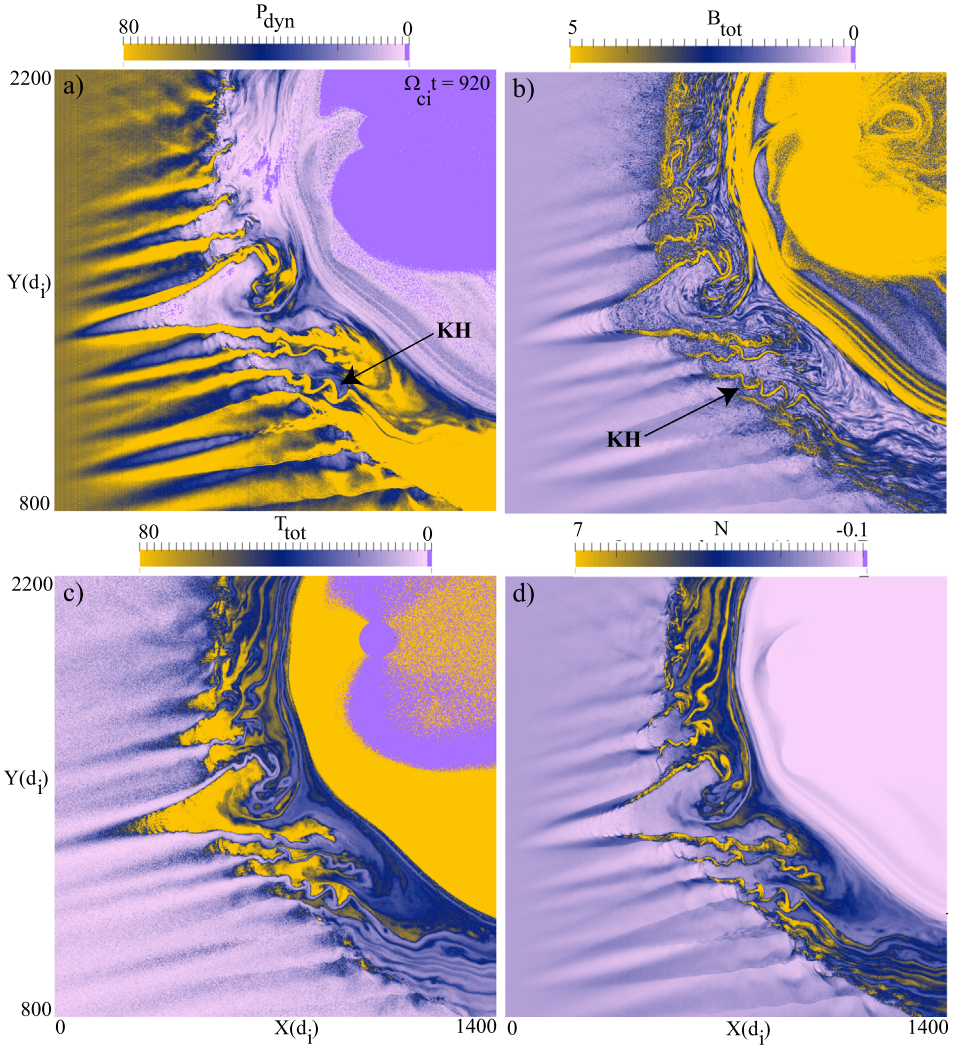

FIG. 16. Properties of the jets (run 1) as shown in plots of (a) dynamical pressure, (b) total magnetic field, (c) total ion temperature, and (d) ion density. The jets exhibit high dynamical pressure, enhanced magnetic field, and density but cooler temperature than their surrounding plasma. The areas between the jets have lower density but hotter plasma in this case.

However, unlike in Figure 19, here this plasma gets caught in the velocity shear in the magnetosheath (Fig. 22(b)) and turns into a vortex (Fig. 22(c)). The color coding of streakline is also useful for tracking the movement of the plasma in different regions of the magnetosheath as seen in Fig. 22(c). The structure in Figure 21(a) has the appearance of a Rayleigh-Taylor finger. The plasma in the jet is denser than the ambient plasma which in the presence of an accelerating force that would mimic gravity could give rise to the Rayleigh-Taylor instability. However, here the formation of this structure appears to be due to dynamics, i.e., deflection of the jet energy as it encounters a nearly perpendicular magnetic field. Although KH driven vortices are known to form on the flanks of the magnetopause (e.g., Ref. 18 and references therein) due to the velocity shear between the solar wind and the magnetopause, we believe this is the first report of a vortex driven due to turbulence in the magnetosheath.

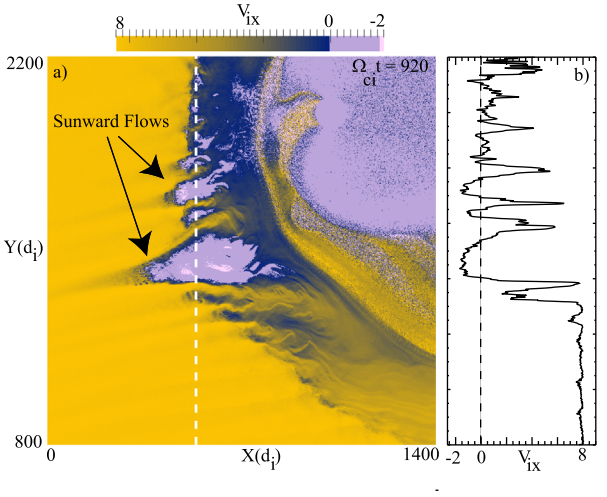

FIG. 17. (a) Plot of V_{ix} for the same simulation time as in Figure 16. Sunward flow regions are associated with the hot regions between the jets in Figure 16(c). (b) The 1D cut shows that the anti-sunward flow in the jets can have speeds comparable to the solar wind whereas the sunward flows can be as high as $2V_A$.

VI. DISCUSSION AND SUMMARY

The fundamental processes of magnetic reconnection, shocks, and turbulence have been demonstrated to be more intimately connected than previously realized. Laminar reconnecting current sheets can develop turbulence;[43] studies of turbulence show that formation of reconnection current sheets may be a generic feature of turbulence in magnetized plasmas (e.g., Refs. 1–5 and references therein). The link between shocks and the other two processes has, until this study, been less clear. For example, one early model of

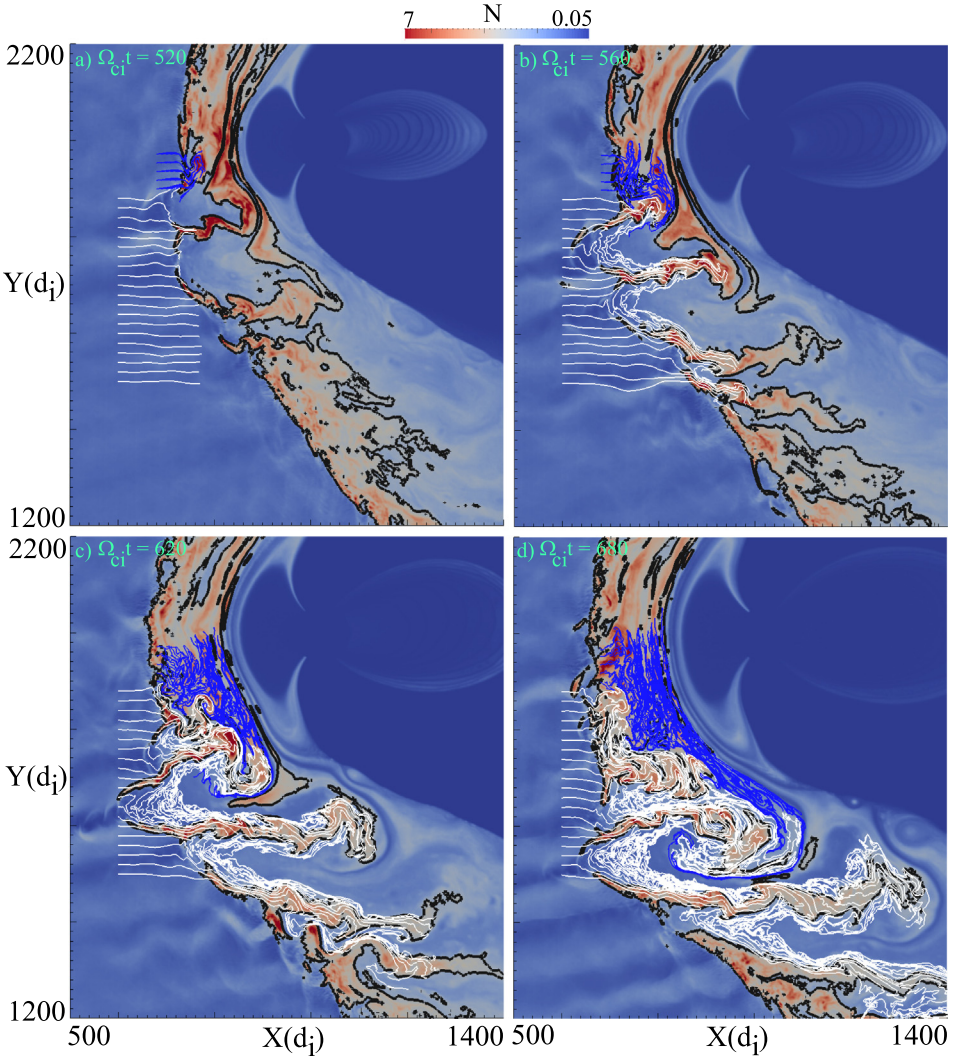

FIG. 18. Sunward flow formation-evolution of the flow associated with the jets is shown with a particular focus on the flow around the bow waves (run 1). Black contours are of density. There is no evidence that interaction of the bow waves/jets with the magnetopause caused a strong sunward flow. Bow waves push the plasma and force it to go around it. This can cause sunward flow. Another way that the bow wave can create a sunward flow is if the jet starts to wrap akin to a vortex. This is evident in panel (d).

reconnection, the Petschek model, required four standing slow shocks as part of the reconnection exhaust.[44] However, the applicability of this model in collisionless plasmas remains in question.[45] Turbulence does not lead to shock formation, except possibly in shear driven turbulence,[3] but even there turbulence is not the cause of shock formation.

Shocks of all types in collisionless plasmas share the property of generating reflected disturbances of electrons and especially ions that can get back upstream into the unshocked medium.[6,46] The angle of upstream magnetic field to the shock normal guides the reflected particles and is one of several parameters controlling the spatial volume to which they may reach before being swept back through the shock layer. In addition, the shock layer substructure may provide for the instability of the transmitted distributions, as is particularly well known for quasi-perpendicular shocks. The turbulence on the downstream side of the shocks reflects the geometry of B to the normal, with the quasi-parallel shocks possessing downstream fluctuations comparable to the mean field and the quasi-perpendicular downstream regions quieter. We have demonstrated for the first time that turbulence associated with the $Q_{\|}$ shocks lead to generation of magnetic islands, with some islands even forming at the shock surface. In some cases (e.g., Fig. 13), the islands can even form ahead of the shock. We have also demonstrated that reflected upstream disturbances when convected back and transmitted through the shock layers eventually dissipate there. Thus, both "waves" and reconnection play a role in providing dissipation downstream of the quasi-parallel shocks. The question of the relative importance of these two processes for dissipation is beyond the scope of this paper and will be addressed elsewhere.

We have thus forged a link between shocks, turbulence, and magnetic reconnection in collisionless plasmas. In doing so, we have provided a theoretical argument that explains the location of reported reconnection events in the magnetosheath.[12,13] Previous studies have not reported the incidence of reconnection in simulations of fast shocks or global hybrid simulations possibly because (i) many fast shock studies were in 1-D where reconnection cannot occur; (ii) the very limited number of 2-D quasi-parallel shock simulations apparently did not check for incidence of reconnection; and (iii) the low number of particles per cell and or low grid resolution of these early simulations (e.g., Ref. 25) may have masked the detection of magnetic islands. Our findings here show that with increasing turbulence levels, the system

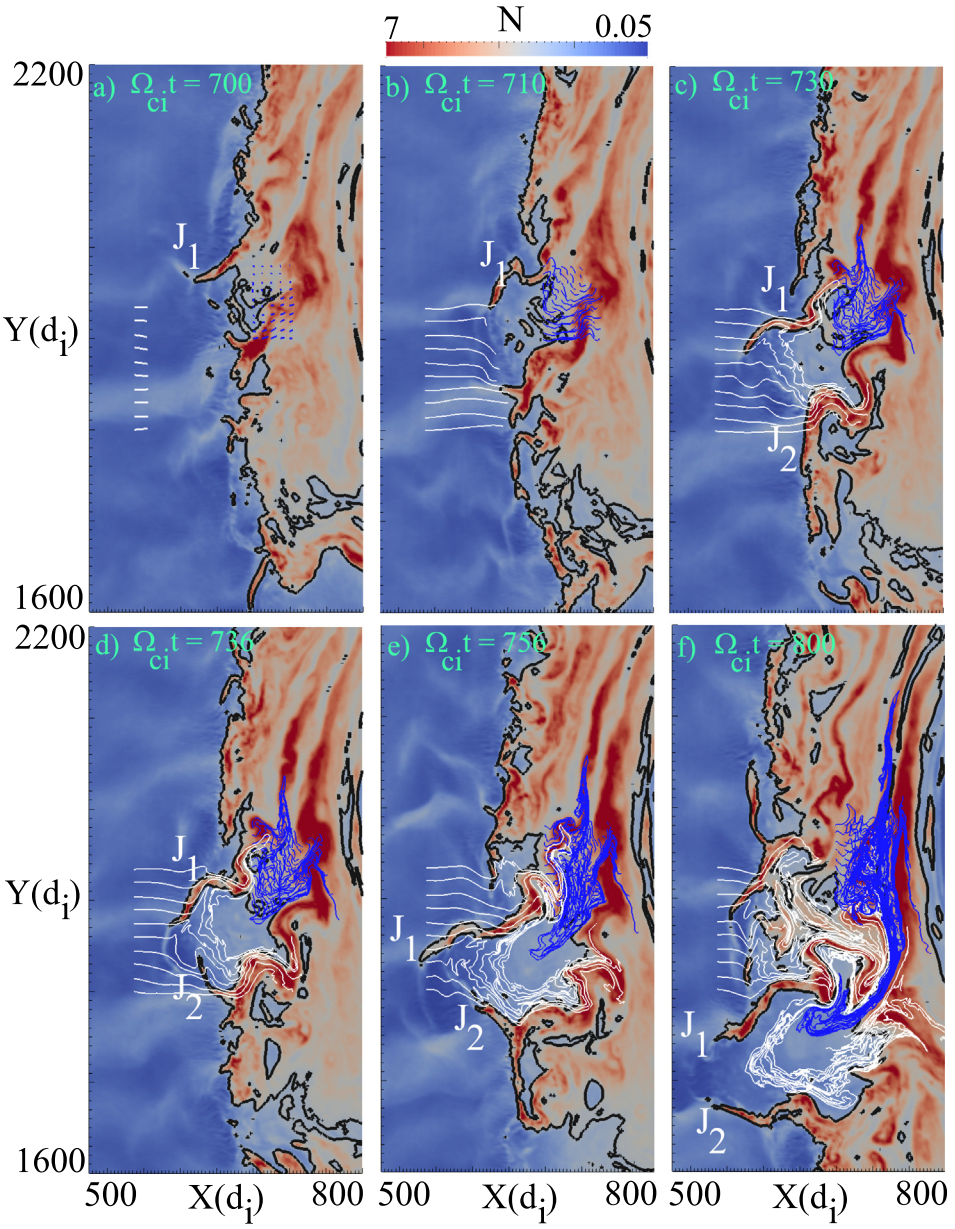

FIG. 19. Sunward flow formation-evolution of the flow associated with the jets with a particular focus on the flow outside of the jets (run 1). Black contours are of density. The jets push the plasma downward into the lower density regions between them as evident from the blue streaklines. The shape and the distance between the jets change on rapid timescales as evident from tracking of two jets, labeled as J_1 and J_2. The flow in the region between the jets can be quite complex.

exhibits greater structural organization in the form of coherent structures such as flux ropes, vortices, and fast jets. Whether such reorganization into coherent structures is a consequence of a general governing principle of all systems far from equilibrium that are driven remains an intriguing speculation.

Another interesting result here is in regards to the large scale consequences of the bow shock turbulence in the magnetosphere. This turbulence can, under certain conditions, enable formation of large scale jets that can interact with the magnetopause and lead to surface waves on it, or inner magnetospheric compressional waves.[11,35,36] The jets can also lead to formation of sunward flows and large scale vortices downstream of the shock.

Given that we found magnetic islands to be a common feature of quasi-parallel shocks with $B_{rms} \sim 1$, search for such structures in the data would be of interest. Ordinarily, flux transfer events are conceptually associated with southward IMF; our simulations have shown examples where flux transfer events can occur with northward IMF along the magnetopause (Fig. 15(b)) as well as inside the magnetosheath (e.g., Fig. 6(b)). While data identified flux transfer events can reach scales of hundreds of d_i, our results demonstrate that flux ropes due to shock "turbulence" appear to be smaller and at most reach tens of d_i in scale.

We have already started the extension of the present work to 3D. Our preliminary results indicate that the basic physical effects uncovered here, such as reconnection in the magnetosheath, remain intact in 3D. However, 3D introduces additional complexity such as fanning of the magnetic field lines in the ion foreshock and formation of Kelvin-Helmholtz instability along the flanks. These results will be reported elsewhere.

ACKNOWLEDGMENTS

This work was partially supported by NASA (NNX12AD30G, Heliophysics Theory), NSF (0904734,

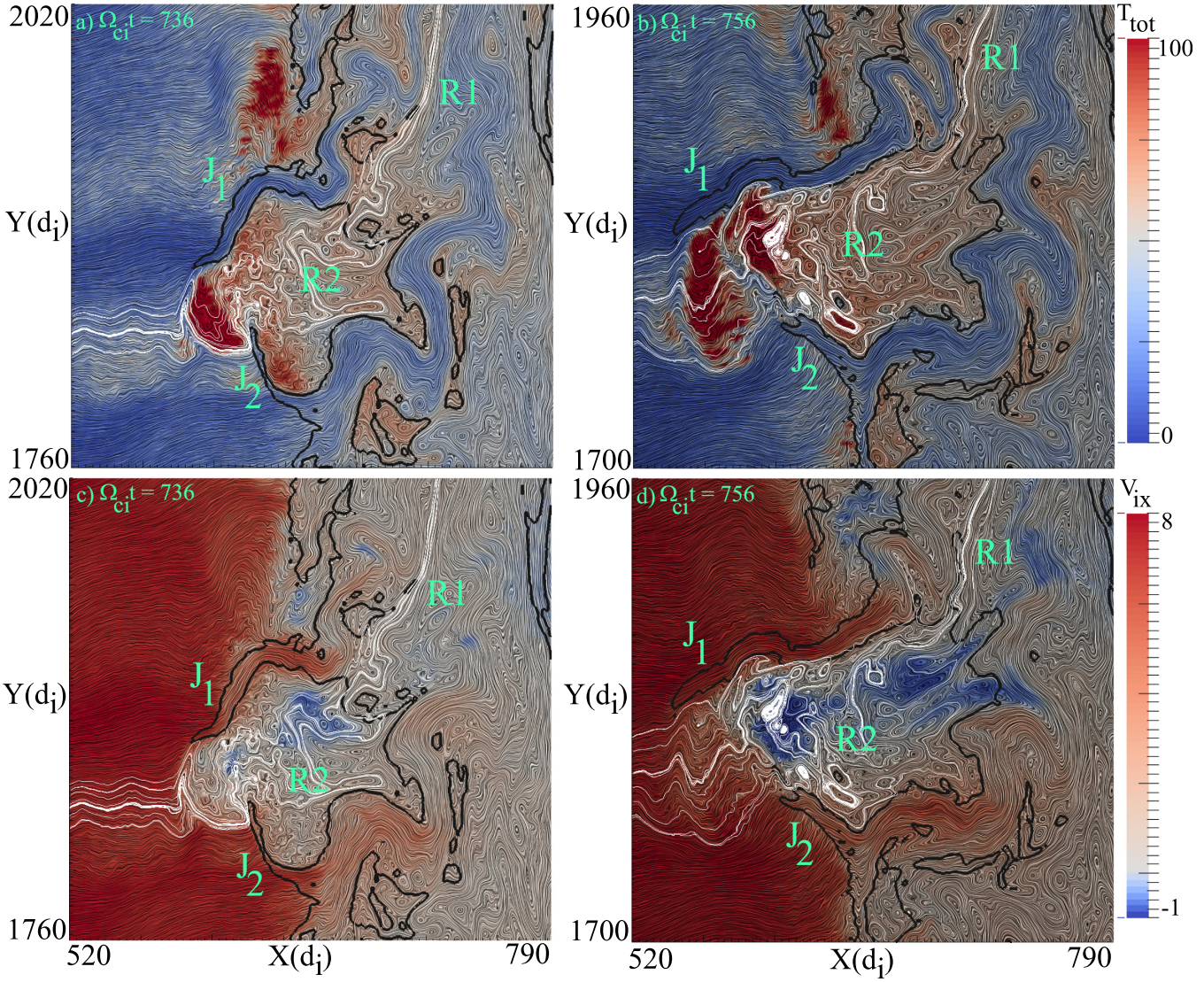

FIG. 20. Close up view of the two jets labeled in Figure 19 as J_1 and J_2. Note the presence of a region of fairly uniform magnetic field between the two jets, marked as $R1$. LIC of magnetic field colored by ion temperature (a)-(b) and (c)-(d) V_{ix} at $\Omega_{ci}t = 736$ and 756. A few magnetic field lines are drawn in white and the black contours are of density. The bow shock surface is clearly rippled. The solar wind plasma penetrates the magnetosheath almost unimpeded along the jets ((c) and (d)) whereas there is strong heating across the shock between the jets as seen in (a) and (b). Note the development of sunward flow as evident from blue regions in (a) and (b). It is mainly driven by the downward flow caused by the jets (blue streaklines in Fig. 19) which push out the plasma between the two jets $R2$.

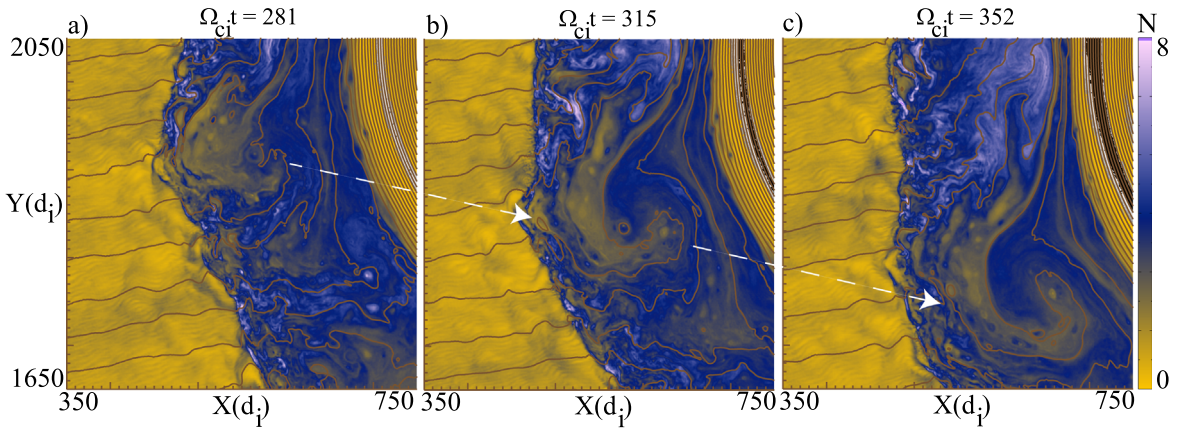

FIG. 21. Nonlinear formation of a large vortex (run 7). Gold curves are magnetic field lines.

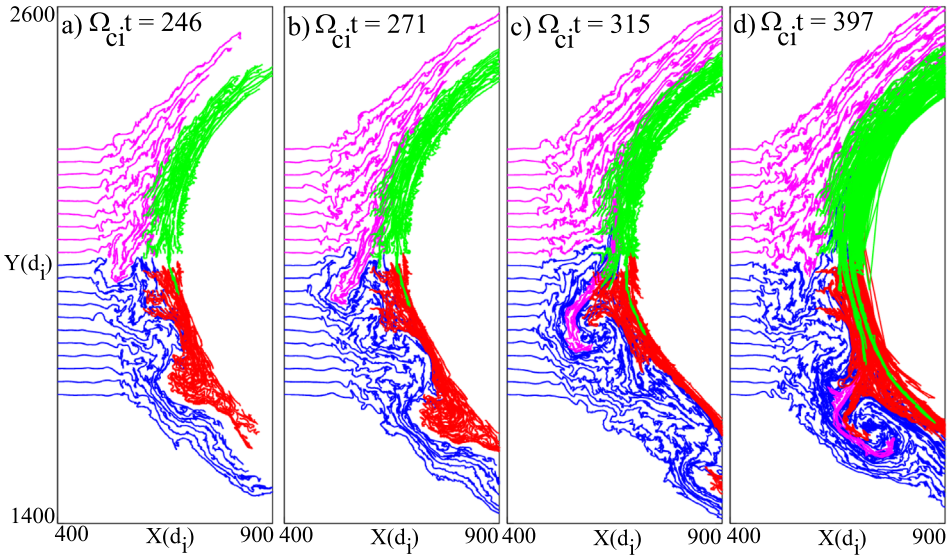

FIG. 22. Development of the vortex in Figure 21 as seen from streaklines. Similar to Figure 19, there is a downward flow (pink streamlines) that pushes the plasma out sunward. In this case, the sunward flow gets caught in the velocity shear in the magnetosheath and wraps up into a vortex.

1104815), and DOE (DE-SC0004662). M.W. acknowledges support from NSF Grants No. AGS-1063439 and No. AGS-1156094 (SHINE), and from NASA Grant No. NNX11AJ44G. JS acknowledges support from NSF ATM 0802380 and NASA NNX07AF40G. Simulations were performed on Pleiades provided by NASA's HEC Program, and Blue Waters sustained-petascale computing project, which is supported by the NSF (OCI 07-25070) and the state of Illinois. We gratefully acknowledge useful discussions with J. Giacalone, J. Borovsky, and A. Retino. We also thank the referee for making useful suggestions that improved the paper.

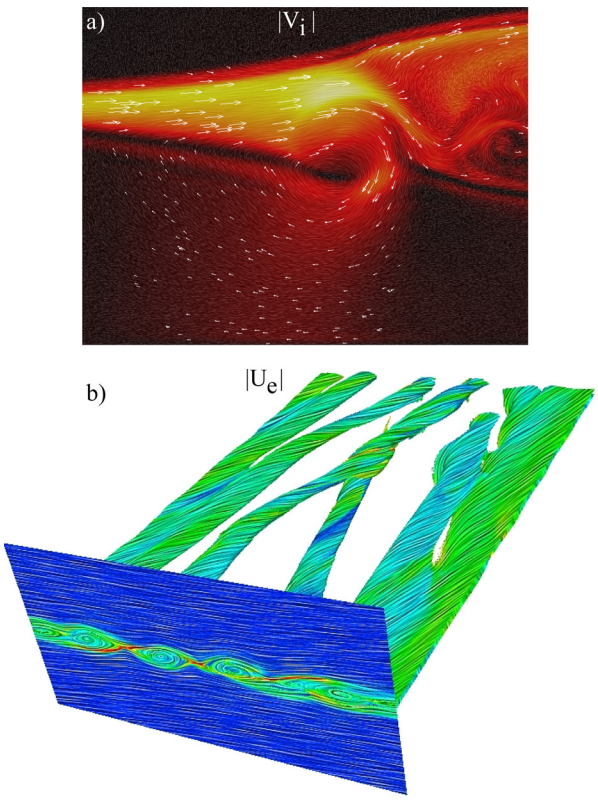

FIG. 23. (a) An example of image LIC. (b) An example of surface LIC. The utility of surface LIC is illustrated using data from a 3D fully kinetic simulation of magnetic reconnection. The 2D projection shows the location of the tearing "islands" which are really flux ropes as evident from the 3D image. The surface of the LIC is defined by isosurface of density and it is colored by electron speed U_e.

APPENDIX A: LINE INTEGRAL CONVOLUTION TECHNIQUE

The standard way to visualize streamlines of a vector field is to seed some points and integrate to trace curves that are instantaneously tangent to the velocity vector. Although useful, this approach can be cumbersome when interactively exploring a dataset. For example, the technique is inherently local and unless feature locations are know *a priori* it is difficult to select an effective set of seed points. An alternative technique called "line integral convolution" or LIC, which convolves noise with a vector field producing streaking patterns that follow vector field tangents, has the advantage that a very detailed view of the streamlines over the entire computational domain is found in one step without the need to explicitly specify a set of seed points.

The technique was initially developed for use on images,[47] but has since been extended to arbitrary surfaces,[48] and to volumes.[49] The algorithm has been ported to the GPU[50] and data-parallel implementations have been developed.[51] We have extended this technique and have made it available through the latest release of ParaView,[52] an open source, cross platform, tool for parallel interactive visualization of large datasets. In addition to traditional visualization algorithms, ParaView provides an MPI based data-parallel GP-GPU surface LIC algorithm which includes a number of enhancements to the basic LIC algorithm designed for interactive data exploration. ParaView's surface LIC can be used on massively parallel supercomputers without GPUs. It is described in detail in ParaView's online documentation.[53] To aid the reader in the interpretation of the figures presented here, a brief review of the LIC algorithm is presented here.

The LIC algorithm of a vector field defined on an image, $I(x,y)$ is given by the following integral over streamline arcs computed from the center of each pixel location, x, y.

$$I(x,y) = \frac{\int_{-L}^{L} k(i)N(S_i)di}{\int_{-L}^{L} k(i)di}, \quad \text{(A1)}$$

where L is the integration length, N generates the noise value at a given location, S_i is a position on a streamline arc centered at x, y, $k(i)$ is an appropriate convolution kernel, and $I(x,y)$ is the image pixel at x, y. In practice, streamline arcs are computed using an RK method over a fixed number of steps, and L can be a constant for all pixels in I, or it may be a function of the local vector field. When L is constant, the resulting visualization has a uniform look. When L varies as a function of the vector local field, the visualization accurately shows relative strengths of flow features. Because the LIC produces a dense representation of the flow field, features of interest can be quickly identified. LIC is often used in conjunction with scalar pseudocoloring. In this case, a specialized shader is used to combine the colors with the gray scale LIC image. Optimized implementations, especially data-parallel or GPU based, are very fast making the technique useful for interactive data exploration.

An example of image LIC of electron stream lines colored by the magnitude of electron velocity is shown in Figure 23(a). The data are from a 2D fully kinetic simulation of asymmetric current sheet. The formation of a vortex associated with a magnetic island (not shown) is clearly evident. The surface LIC technique we use is similar to image based LIC except first vectors are projected onto the surface then into image space where an image LIC algorithm is used to compute LIC.[48] Lit, pseudocolored surface geometry, is combined with the image LIC to produce a realistic rendering of the surface geometry. To show the utility of surface LIC in analysis of 3D data, we have applied it to data from a 3D fully kinetic simulation of reconnection.[43] Figure 23(b), using isocontour of density, shows the presence of multiple flux ropes as evident from their helical magnetic field lines.

[1]W. H. Matthaeus and S. L. Lamkin, Phys. Fluids **28**, 303 (1985).
[2]S. Servidio, P. Dmitruk, A. Greco, M. Wan, S. Donato, P. A. Cassak, M. A. Shay, V. Carbone, and M. Matthaeus, Nonlinear Process. Geophys. **18**, 675 (2011).
[3]H. Karimabadi, V. Roytershteyn, M. Wan, W. H. Matthaeus, W. Daughton, P. Wu, M. Shay, B. Loring, J. Borovsky, E. Leonardis *et al.*, Phys. Plasmas **20**, 012303 (2013).
[4]H. Karimabadi, V. Roytershteyn, W. Daughton, and Y.-H. Lin, Space Sci. Rev. **178**, 307–323 (2013).
[5]H. Karimabadi and A. Lazarian, Phys. Plasmas **20**, 112102 (2013).
[6]D. Burgess *et al.*, Space Sci. Rev. **118**, 205 (2005).
[7]B. Lembege and J. Dawson, Phys. Fluids **30**, 1767 (1987).
[8]O. Alexandrova, Nonlinear Processes Geophys. **15**, 95 (2008).
[9]H. Hietala, T. V. Laitinen, K. Andreov, R. Vainio, A. Vaivads, M. Palmroth, T. I. Pulkkinen, H. E. J. Koskinen, E. A. Lucek, and H. Rme, Phys. Rev. Lett. **103**, 245001 (2009).
[10]H. Hietala and F. Plaschke, J. Geophys. Res. **118**, 7237, doi:10.1002/2013JA019172 (2013).
[11]J.-H. Shue, J.-K. Chao, P. Song, J. P. McFadden, A. Suvorova, V. Angelopoulos, and F. Plaschke, Geophys. Res. Lett. **36**, L18112, doi:10.1029/2009GL039842 (2009).
[12]A. Retino, D. Sundkvist, A. Vaivads, F. S. Mozer, M. Andr, and C. Owen, Nature Phys. **3**, 236 (2007).
[13]D. Sundkvist, A. Retino, A. Vaivads, and S. D. Bale, Phys. Rev. Lett. **99**, 025004 (2007).
[14]B. Sonnerup, H. Hasegawa, W.-L. Teh, and L.-N. Hau, J. Geophys. Res. **111**, A09204, doi:10.1029/2006JA011717 (2006).
[15]H. Hasegawa, R. Nakamura, M. Fujimoto, V. A. Sergeev, E. A. Lucek, H. Rème, and Y. Khotyaintsev, J. Geophys. Res. **112**, A11206, doi:10.1029/2007JA012492 (2007).
[16]C. Russell and R. C. Elphic, Geophys. Res. Lett. **6**, 33, doi:10.1029/GL006i001p00033 (1979).
[17]H. Hasegawa, M. Fujimoto, T.-D. Phan, H. Reme, A. Balogh, M. W. Dunlop, C. Hashimoto, and R. TanDokoro, Nature **430**, 755 (2004).
[18]T. Nakamura, W. Daughton, H. Karimabadi, and S. Eriksson, J. Geophys. Res. **118**, 5742, doi:10.1002/jgra.50547 (2013).
[19]H. Karimabadi, H. X. Vu, D. Krauss-Varban, and Y. Omelchenko, in *Proceedings of the Conference on the Numerical Modeling of Space Plasma Flows: Astronum-2006, Palm Springs, CA, 26–30 March 2006*, ASP Conference Series Volume 359, edited by N. V. Pogorelov and G. P. Zank (Astronomical Society of the Pacific, San Francisco, CA), p. 257.
[20]H. Karimabadi, B. Loring, H. X. Vu, Y. Omelchenko, M. Tatineni, A. Majumdar, U. Ayachit, and B. Geveci, in *5th International Conference of Numerical Modeling of Space Plasma Flows, Proceedings of a 5th International Conference Held at San Diego, California, USA, edited by Nikolai V. Pogorelov, 13-18 June 2010* (Astronomical Society of the Pacific, San Francisco, 2011), p. 281.
[21]H. Karimabadi, P. Oleary, T. Mahidhar, B. Loring, A. Majumdar, and B. Geveci, in *XSEDE13 Extreme Science and Engineering Discovery Environment: Gateway to Discovery San Diego, CA, USA, 22–25 July* (New York, NY, 2013), ACM 978-1-4503-2170-9/13/07, p. 257.
[22]J. D. Scudder and S. Olbert, J. Geophys. Res. **84**, 6603, doi:10.1029/JA084iA11p06603 (1979).
[23]E. Sittler and J. D. Scudder, J. Geophys. Res. **85**, 5131, doi:10.1029/JA085iA10p05131 (1980).
[24]N. Omidi, X. Blanco-Cano, C. Russell, and H. Karimabadi, Adv. Space Res. **33**, 1996 (2004).
[25]N. Omidi, J. Eastwood, and D. G. Sibeck, J. Geophys. Res. **115**, A06204, doi:10.1029/2009JA014828 (2010).
[26]D. Turner, N. Omidi, D. G. Sibeck, and V. Angelopoulos, J. Geophys. Res. **118**, 1552, doi:10.1002/jgra.50198 (2013).
[27]J. Giacalone, D. Burgess, S. Schwartz, and D. Ellison, Geophys. Res. Lett. **19**, 433, doi:10.1029/92GL00379 (1992).
[28]J. Giacalone, Astrophys. J. **609**, 452 (2004).
[29]J. Giacalone, Astrophys. J. **628**, L37 (2005).
[30]L. Burlaga, Sol. Phys. **7**, 54 (1969).
[31]A. P. Dimmock and K. Nykyri, J. Geophys. Res. **118**, 4963, doi:10.1002/jgra.50465 (2013).
[32]K. J. Bowers, B. J. Albright, L. Yin, B. Bergen, and T. J. T. Kwan, Phys. Plasmas **15**, 055703 (2008).
[33]L. Shan, L. Quanming, M. Wu, X. Gao, C. Huang, T. Zhang, and W. Shui, J. Geophys. Res. **119**, 237–245, doi:10.1002/2013JA019396 (2014).
[34]L. Prech, Z. Nemecek, and J. Safrankova, Earth Planets Space **61**, 607 (2009).
[35]E. Amata, S. P. Savin, D. Ambrosino, Y. V. Bogdanova, M. F. Marcucci, S. Romanov, and A. Skalsky, Planet. Space Sci. **59**, 482 (2011).
[36]F. Plaschke, K.-H. Glassmeier, D. Sibeck, H. U. Auster, O. D. Constantinescu, V. Angelopoulos, and W. Magnes, Ann. Geophys. **27**, 4521 (2009).
[37]Z. Němeček, J. Šafránková, L., Přech, D. G. Sibeck, S. Kokubun, and T. Mukai, Geophys. Res. Lett. **25**, 1273, doi:10.1029/98GL50873 (1998).
[38]S. Savin, E. Amata, L. Zelenyi, V. Budaev, G. Consolini, R. Treumann, E. Lucek, J. Safrankova, Z. Nemecek, Y. Khotyaintsev *et al.*, JETP Lett. **593**, 87 (2008).
[39]M. O. Archer and T. S. Horbury, Ann. Geophys. **31**, 319 (2013).
[40]F. Plaschke, H. Hietala, and V. Angelopoulos, Ann. Geophys. **31**, 1877 (2013).
[41]J. T. Gosling, M. F. Thomsen, S. J. Bame, and C. T. Russell, J. Geophys. Res. **94**, 10027, doi:10.1029/JA094iA08p10027 (1989).
[42]S. Savin, E. Amata, L. Zelenyi, V. Lutsenko, J. Safrankova, Z. Nemecek, N. Borodkova, J. Buechner, P. W. Daly, E. A. Kronberg *et al.*, Ann. Geophys. **30**, 1 (2012).
[43]W. Daughton, V. Roytershteyn, H. Karimabadi, L. Yin, B. J. Albright, B. Bergen, and K. J. Bowers, Nature Phys. **7**, 539 (2011).
[44]H. Petschek, in *Proceedings of the AAS-NASA Symposium held 2830 October 1963 at the Goddard Space Flight Center, Greenbelt, MD* (1964), p. 425.

[45]A. Le, J. Egedal, J. Ng, J. H. Karimabadi, J. Scudder, V. Roytershteyn, W. Daughton, and Y.-H. L. Liu, Phys. Plasmas **21**, 012103 (2014).
[46]H. Karimabadi, D. Krauss-Varban, and N. Omidi, J. Geophys. Res. **100**, 11957, doi:10.1029/94JA03035 (1995).
[47]B. Cabral and L. Leedom, in *SIGGRAPH'93* (1993), p. 263.
[48]R. Laramee, B. Jobard, and H. Hauser, in *Visualization, 2003. VIS 2003* (IEEE, 2003), p. 131.
[49]V. Interrante and C. Grosch, in *Proceedings of the 8th Conference on Visualization, VIS '97* (IEEE Computer Society Press, Los Alamitos, CA, USA, 1997), pp. 421–ff.
[50]D. Weiskopf, *GPU-Based Interactive Visualization Techniques (Mathematics and Visualization)* (Springer-Verlag, Inc., New York; Secaucus, NJ, 2006).
[51]S. Bachthaler, M. Strengert, D. Weiskopf, and T. Ertl, In Proceeding of Eurographics Symposium on Parallel Graphics and Visualization, EGPGV 2006, Braga, Portugal, 2006.
[52]A. Henderson, *ParaView Guide, A Parallel Visualization Application* (Kitware, Inc., 2005).
[53]Paraview, see http://paraview.org/Wiki/ParaView/Line_Integral_Convolution (2014).